Evaluation of cloud-resolving and limited area model intercomparison simulations using TWP-ICE observations: 1. Deep convective updraft properties

Adam Varble, Edward J Zipser, Ann M Fridlind, Ping Zhu, Andrew S Ackerman, Jean-pierre Chaboureau, Scott Collis, Jiwen Fan, Adrian Hill, Ben Shipway

AGU PUBLICATIONS

JGR

Journal of Geophysical Research: Atmospheres

RESEARCH ARTICLE
10.1002/2013JD021371

This article is a companion to *Varble et al.* [2014] doi:10.1002/2013JD021372.

Key Points:
- High biased simulated convective dBZ partly results from overly intense updrafts
- Lofted large simulated rainwater contents produce excessive vertical velocities
- Increasing resolution does not completely solve simulation biases

Supporting Information:
- Readme
- Animation S1
- Animation S2

Correspondence to:
A. Varble,
a.varble@utah.edu

Citation:
Varble, A., E. J. Zipser, A. M. Fridlind, P. Zhu, A. S. Ackerman, J.-P. Chaboureau, S. Collis, J. Fan, A. Hill, and B. Shipway (2014), Evaluation of cloud-resolving and limited area model intercomparison simulations using TWP-ICE observations: 1. Deep convective updraft properties, *J. Geophys. Res. Atmos.*, *119*, 13,891–13,918, doi:10.1002/2013JD021371.

Received 17 DEC 2013
Accepted 7 OCT 2014
Accepted article online 13 OCT 2014
Published online 18 DEC 2014

Evaluation of cloud-resolving and limited area model intercomparison simulations using TWP-ICE observations: 1. Deep convective updraft properties

Adam Varble[1], Edward J. Zipser[1], Ann M. Fridlind[2], Ping Zhu[3], Andrew S. Ackerman[2], Jean-Pierre Chaboureau[4], Scott Collis[5], Jiwen Fan[6], Adrian Hill[7], and Ben Shipway[7]

[1]Department of Atmospheric Sciences, University of Utah, Salt Lake City, Utah, USA, [2]NASA Goddard Institute for Space Studies, New York, New York, USA, [3]Department of Earth Sciences, Florida International University, Miami, Florida, USA, [4]Laboratoire d'Aerologie, University of Toulouse/CNRS, Toulouse, France, [5]Environmental Science Division, Argonne National Laboratory, Argonne, Illinois, USA, [6]Department of Climate Physics, Pacific Northwest National Laboratory, Richland, Washington, USA, [7]Met Office, Exeter, UK

Abstract Ten 3-D cloud-resolving model simulations and four 3-D limited area model simulations of an intense mesoscale convective system observed on 23–24 January 2006 during the Tropical Warm Pool-International Cloud Experiment (TWP-ICE) are compared with each other and with observed radar reflectivity fields and dual-Doppler retrievals of vertical wind speeds in an attempt to explain published results showing a high bias in simulated convective radar reflectivity aloft. This high-bias results from ice water content being large, which is a product of large, strong convective updrafts, although hydrometeor size distribution assumptions modulate the size of this bias. Making snow mass more realistically proportional to D^2 rather than D^3 eliminates unrealistically large snow reflectivities over 40 dBZ in some simulations. Graupel, unlike snow, produces high biased reflectivity in all simulations, which is partly a result of parameterized microphysics but also partly a result of overly intense simulated updrafts. Peak vertical velocities in deep convective updrafts are greater than dual-Doppler-retrieved values, especially in the upper troposphere. Freezing of liquid condensate, often rain, lofted above the freezing level in simulated updraft cores greatly contributes to these excessive upper tropospheric vertical velocities. The strongest simulated updraft cores are nearly undiluted, with some of the strongest showing supercell characteristics during the multicellular (presquall) stage of the event. Decreasing horizontal grid spacing from 900 to 100 m slightly weakens deep updraft vertical velocity and moderately decreases the amount of condensate aloft but not enough to match observational retrievals. Therefore, overly intense simulated updrafts may additionally be a product of unrealistic interactions between convective dynamics, parameterized microphysics, and large-scale model forcing that promote different convective strengths than observed.

1. Introduction

Properly modeling tropical deep convective systems is critical to predicting both weather and climate, but doing so currently remains one of the greatest challenges in atmospheric science. The proportion of convective to stratiform precipitation is vital to accurately represent the heating effects of mesoscale precipitation systems, which account for a large fraction of tropical rainfall [*Del Genio and Kovari*, 2002; *Houze*, 2004] and strongly impact large-scale dynamics by controlling the distribution of free tropospheric heating [*Houze*, 1982, 1989, 1997, 2004; *Hartmann et al.*, 1984; *Johnson*, 1984; *Schumacher et al.*, 2004]. Unfortunately, mesoscale simulations run on cloud-resolving horizontal scales down to 1 km often fail to reproduce observed convective and stratiform structures [e.g., *Lang et al.*, 2003; *McFarquhar et al.*, 2006; *Zhou et al.*, 2007; *Luo et al.*, 2010; *Varble et al.*, 2011] that depend on the large-scale environmental properties [*Houze*, 2004]. A primary source of error in these simulations is parameterization of subgrid-scale microphysical processes, which are often poorly constrained and quite crude [*Tao and Moncrieff*, 2009]. Despite uncertainties in these parameterizations, cloud-resolving models (CRMs) are increasingly used in satellite algorithms [e.g., *Kummerow et al.*, 2001; *Kingsmill et al.*, 2004; *Shige et al.*, 2009] to derive quantities such as rainfall and latent heating. They are also used to guide general circulation model (GCM) cloud and convective parameterization improvement [e.g., *Tiedtke*, 1993; *Lohmann and Roeckner*, 1996; *Fowler et al.*, 1996; *Ghan et al.*, 1997; *Rotstayn*, 1997; *Wilson and Ballard*, 1999; *Del Genio et al.*, 2012], as

these parameterizations are large sources of error in GCMs [*Randall et al*., 2003]. With increased computing ability in the past decade, some have even begun embedding 2-D CRMs in GCM grid boxes, a process known as superparameterization [*Grabowski*, 2001; *Khairoutdinov and Randall*, 2001; *Randall et al*., 2003].

One approach for constraining parameterized processes in modeling is to compare high-quality in situ and remote-sensing observations to output from several cloud-resolving simulations that use the same large-scale forcing but different parameterizations. This approach, referred to as an intercomparison, has been used for several different deep convective field experiments [e.g., *Wu et al*., 1998; *Redelsperger et al*., 2000; *Xu et al*., 2002; *Bryan et al*., 2006; *Grabowski et al*., 2006] including the Tropical Warm Pool-International Cloud Experiment (TWP-ICE) [*Fridlind et al*., 2012]. This approach has also been extensively used for single-column models [e.g., *Bechtold et al*., 2000; *Ghan et al*., 2000; *Wu and Moncrieff*, 2001; *Xie et al*., 2002; *Davies et al*., 2013] and has recently been extended to limited area models (LAMs) for TWP-ICE [*Zhu et al*., 2012]. TWP-ICE was based out of Darwin, Australia in January and February of 2006 during the heart of the wet monsoon season and consisted of active, suppressed, and break monsoon periods. Large-scale conditions during the active period are similar to tropical maritime conditions, while conditions during the break period are more continental with less rainfall but more intense convection [*Cifelli and Rutledge*, 1998; *May and Ballinger*, 2007]. A detailed description of the experiment is given in *May et al*. [2008].

The active monsoon period during TWP-ICE covered 19–25 January 2006 and included several significant mesoscale precipitation events. With a focus on this period, *Varble et al*. [2011] compared convective and stratiform structures between nine different 3-D CRM simulations and observations using C band radar reflectivity and satellite-observed infrared brightness temperatures. The time series of total precipitation was well captured by the CRMs, but the separation of precipitating areas into convective and stratiform regions showed substantial differences from observations. Despite a spread in model results and a suite of different microphysics schemes, all simulations significantly underestimated stratiform rain rates and overestimated convective radar reflectivity above the freezing level. It was found that differences in simulated radar reflectivity in the convective and stratiform regions primarily resulted from different size distribution assumptions in the various bulk microphysics schemes employed.

Several studies show that cloud-resolving simulations overestimate radar reflectivity aloft in convective regions of tropical oceanic convection due to excessive amounts of large graupel [*Blossey et al*., 2007; *Lang et al*., 2007; *Li et al*., 2008; *Matsui et al*., 2009; *Caine et al*., 2013]. *Varble et al*. [2011] agreed that this was the case for most CRM simulations of TWP-ICE active monsoonal convection, but that snow in addition to graupel could cause the high bias in two-moment schemes. The possible contribution of simulated vertical velocity (w) biases to microphysics biases has not been thoroughly explored. One exception is *Lang et al*. [2007], who concluded that maximum CRM-simulated vertical velocities in tropical convection were similar to dual-Doppler-retrieved values; however, they did not isolate and analyze statistical properties of deep updraft cores in their analysis. Modeling studies of tropical oceanic deep convection such as *Zeng et al*. [2008] show that peak upper tropospheric w values greater than 30 m s^{-1} with large cloud water and graupel mass are common, but these values are not supported by observations in similar meteorological regimes. Using ground-based vertical profilers at Darwin, *May and Rajopadhyaya* [1999] found a 90th percentile maximum w of 8 m s^{-1} at 5 km and 11 m s^{-1} at 10 km. Their statistics included shallow and decaying updrafts in addition to mature updrafts; however, purely deep updraft statistics (cores greater than 10 km in extent) in a near-coastal site in India [*Uma and Narayana Rao*, 2008] show similar peak values of 15 m s^{-1} in the upper troposphere with values of ~10 m s^{-1} at 4–5-km altitudes. Using nadir-viewing airborne Doppler radar overflying overshooting convection in near-coastal environments, *Heymsfield et al*. [2010] found that peak w values greater than 30 m s^{-1} rarely occurred in any of the tropical or subtropical environments sampled, including those over land.

This paper is part of a two-part manuscript evaluating 10 CRM and four LAM simulations of an intense active monsoonal mesoscale convective system (MCS) against observational retrievals. Utilizing scanning radar retrievals of vertical wind speed and reflectivity, Part 1 provides evidence for high biased convective radar reflectivity and area partly originating in simulated convective updrafts with high biased vertical velocities and condensate. Part 2 explores sources for the low bias in simulated stratiform rainfall described in *Varble et al*. [2011] using rain microphysics retrievals and results found in Part 1. The effect of model forcing on simulation biases is explored (primarily in Part 2) by comparing both CRM and LAM simulations to observations.

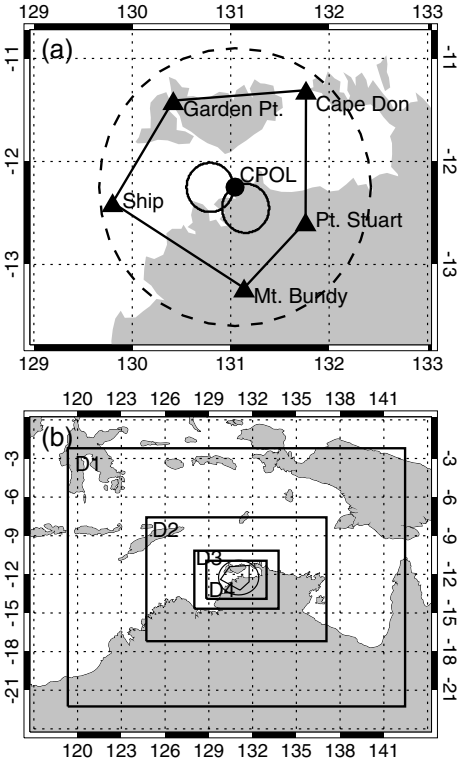

Figure 1. (a) The five boundary-sounding sites that define the pentagonal forcing domain for the CRMs. The location of the CPOL radar, its 150-km range ring (dashed), and the dual-Doppler retrieval lobes are also shown. (b) The four nested LAM domains with the innermost D4 encompassing the CPOL range ring and CRM forcing area shown in Figure 1a.

2. Models

2.1. CRM Simulations

In this study, CRM refers to a model using a single domain with an idealized oceanic lower boundary and doubly periodic lateral boundary conditions forced with advective tendencies derived from a variational analysis constructed from available observations [see *Xie et al*., 2010]. Ten 3-D simulations spanning 3*Z* 23 January to 12*Z* 24 January 2006 were performed using four different models: the Distributed Hydrodynamic-Aerosol-Radiation-Microphysics Application (DHARMA) [*Ackerman et al*., 2000; *Stevens et al*., 2002], the Meso-NH Atmospheric Simulation System (MESONH) [*Lafore et al*., 1998], the UK Met Office Large Eddy Model (UKMO) [*Shutts and Gray*, 1994; *Petch and Gray*, 2001], and the System for Atmospheric Modeling (SAM) [*Khairoutdinov and Randall*, 2003]. Six setups: DHARMA-B, DHARMA-S, MESONH-1, MESONH-2, SAM-B, and SAM-S, are exactly the same as in *Varble et al*. [2011] and were run as restart simulations of longer simulations started at 0*Z* 18 January 2006, as described further in *Varble et al*. [2011] and *Fridlind et al*. [2012]. The SAM simulations are unique with respect to other simulations in that they use hail with a density of 900 kg m^{-3} as the precipitating dense ice species rather than graupel with a density of 400 kg m^{-3}. For these simulations, the difference between graupel and hail is in density and fall speed rather than size or growth mode, as might typically be used as separators in observations. The remaining three setups in *Varble et al*. [2011]: UKMO-1, UKMO-2, and UKMO-2 M, are altered from the simulations in *Varble et al*. [2011] to have higher vertical resolution on par with other simulations. Furthermore, a tenth setup referred to as DHARMA-2 M is added, also restarted from a longer simulation beginning at 0*Z* 18 January 2006. This simulation uses a recent version of the Morrison microphysics scheme [*Morrison et al*., 2009] modified to include prognostic cloud water number concentration (*N*) that uses idealized aerosol *N* profiles in three size modes based on observations from the Aerosol and Chemical Transport in tropical convection (ACTIVE) field campaign [*Vaughan et al*., 2008], which took place at Darwin, Australia and included the TWP-ICE period. The SAM simulations use these aerosol size distributions as well, but DHARMA-2 M is unique in that it accounts for aerosol transport and consumption. Model forcing is derived using a variational method incorporating several observations including 3-hourly soundings at five sites and radar-retrieved precipitation [*Xie et al*., 2010]. The forcing is derived within the pentagon defined by the five sounding sites shown in Figure 1a. Also shown in Figure 1a is the CPOL radar domain, signified by a 150 km range ring. Lateral boundaries are periodic and the lower boundary is oceanic with a constant sea surface temperature of 29°C. Because of the active monsoonal nature of this precipitation, land effects are assumed to be limited despite significant land area within the forcing domain. Table 1 gives the domain size, horizontal and vertical resolution, and microphysics schemes used in each simulation, as well as descriptions of the symbols used to represent each simulation in the figures to follow. The domain sizes are common for model intercomparisons and are used because they are analogous to the approximate size of GCM grid boxes and can make use of the large-scale forcing derived from the variational analysis. In this way, CRM output is comparable to single-column model output; however, these domain sizes are potentially too small to properly represent cloud and precipitation statistical properties of large MCS cases such as the one in this study, as is discussed in greater detail in Part 2. Output from simulations was saved every 10 min yielding 199 output times. Further information on the model specifications can be found in *Fridlind et al*. [2010], *Varble et al*. [2011], and *Fridlind et al*. [2012].

Table 1. The Configurations of the 10 CRM Simulations Including the Symbols Used in the Figures[a]

CRM Simulation Configurations					
Simulation	Symbol	Domain	Δx (m)	Δz (m)	Microphysics
DHARMA-B	Filled Diamond	$(176\ km)^2$	917	100–250	One moment [*Grabowski*, 1999]
DHARMA-S	Open Diamond	$(176\ km)^2$	917	100–250	One moment
DHARMA-2 M	x	$(176\ km)^2$	917	100–250	Two moment (i,w,r,g,s) [*Morrison et al*., 2009]
UKMO-1	Right pointing Triangle	$(177\ km)^2$	917	100–250	Two moment (i) [*Gray et al*., 2001]
UKMO-2	Left pointing Triangle	$(177\ km)^2$	917	100–250	Two moment (i,g,s) [*Gray et al*., 2001]
UKMO-2 M	Square	$(177\ km)^2$	917	100–250	Two moment (i,r,g,s) [*Morrison et al*., 2009]
MESONH-1	Up pointing Triangle	$(192\ km)^2$	1000	100–250	One moment [*Pinty and Jabouille*, 1998]
MESONH-2	Down pointing Triangle	$(192\ km)^2$	1000	100–250	Two moment (i,w) [*Pinty*, 2002]
SAM-B	Filled Circle	$(192\ km)^2$	1000	100–400	Two moment (i,w,r,h,s) [*Morrison et al*., 2009]
SAM-S	Open Circle	$(192\ km)^2$	1000	100–400	Two moment (i,w,r,h,s)

[a]Baseline simulations are represented by filled symbols and sensitivity simulations are represented by open symbols. Sensitivity simulations differ from baseline simulations in that they use a 6 h nudging of domain mean potential temperature and water vapor in the free troposphere. If a simulation has two-moment species, then they are indicated in parentheses: i, cloud ice; w, cloud water; r, rain; g, graupel; h, hail; and s, snow.

2.2. LAM Simulations

Horizontal and vertical grid spacing in the LAMs is similar to that in the CRMs, but the LAMs are forced by the European Centre for Medium-Range Forecasts (ECMWF) global operational analyses through their horizontal boundaries using two-way nesting and have an inhomogeneous surface that includes variable land and ocean properties. The LAM simulations used in this study include three Advanced Research Weather Research and Forecasting (WRF-ARW) V3.1.1 model [*Skamarock et al*., 2008] runs described as WRF-1, WRF-2, and WRF-3 in the TWP-ICE LAM intercomparison study [*Zhu et al*., 2012] and referred to as WRF-W, WRF-T, and WRF-M in this study. Shown in Figure 1b, the outer domain (D1) has a horizontal grid spacing of 27 km, and the inner domain (D4) has a horizontal grid spacing of 1 km. D2 and D3 have horizontal grid spacing of 9 and 3 km, respectively. D4 covers 450 km by 330 km. ECMWF analysis nudging of tropospheric horizontal winds, temperature, and water vapor mixing ratio is used in D1, D2, and D3 using a nudging time scale of ~1 h with linearly interpolated analyses.

All three simulations share the same setup except for their use of different microphysics schemes shown in Table 2. WRF-M uses the Morrison scheme [*Morrison et al*., 2009], WRF-W the WSM6 scheme [*Hong and Lim*, 2006], and WRF-T the Thompson scheme [*Thompson et al*., 2008]. Each scheme uses five hydrometeor species. The WRF Morrison scheme predicts the mass mixing ratio of rain, graupel, snow, cloud ice, and cloud water in addition to the number concentration of rain, graupel, snow, and cloud ice. The Thompson scheme predicts the mass mixing ratio of rain, graupel, snow, cloud ice, and cloud water in addition to the number concentration of rain and cloud ice. The graupel size intercept (N_0) varies as a function of mass mixing ratio to mimic the transition from lightly rimed snow to hail [*Thompson et al*., 2008]. Snow is represented by a combination of two gamma size distributions that vary as a function of temperature described in *Field et al*. [2005]. Furthermore, the snow mass-diameter (*m-D*) relationship assumes nonspherical particles based on the relationship in *Cox* [1988], whereas the Morrison and WSM6 schemes assume spherical, constant density *m-D* relationships. The WSM6 scheme is purely a one-moment scheme with prognostic rain, graupel, snow, cloud ice, and cloud water mass mixing ratios, with snow N_0 varying diagnostically as a function of temperature using a relationship from *Houze et al*. [1979]. Other model physics schemes used in all LAM

Table 2. The Configurations of the Four LAM Simulations Including the Symbols Used in the Figures[a]

LAM Simulation Configurations					
Simulation	Symbol	Domain (D4)	Δx (m)	Δz (m)	Microphysics
WRF-W	Triangle	450 km × 330 km	1000	~100–300	One moment [*Hong et al*., 2006]
WRF-T	Square	450 km × 330 km	1000	~100–300	Two moment (r) [*Thompson et al*., 2008]
WRF-M	Diamond	450 km × 330 km	1000	~100–300	Two moment (i,r,g,s) [*Morrison et al*., 2009]
WRF-M2	Dashed Line	450 km × 330 km	1000	~100–300	Two moment (i,r,g,s) [*Morrison et al*., 2009]

[a]If a simulation has two-moment species, then they are indicated in parentheses: i, cloud ice; r, rain; g, graupel; and s, snow.

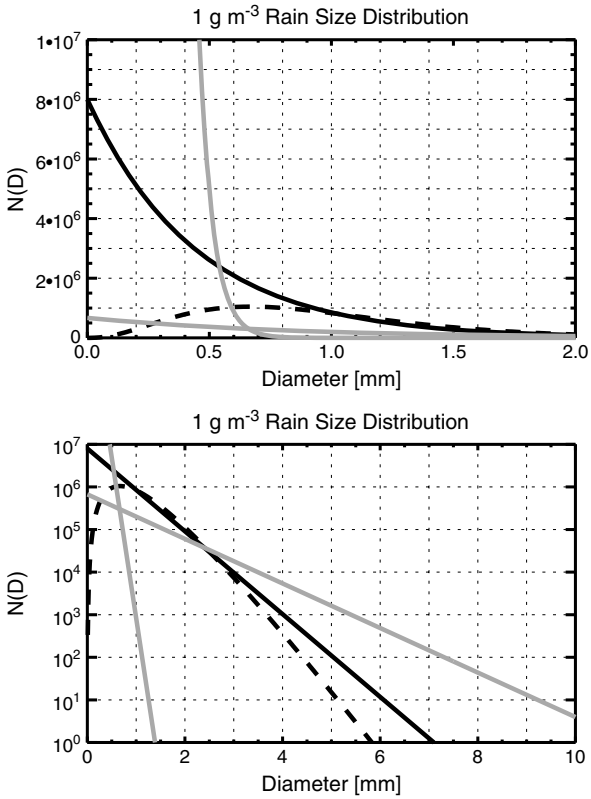

Figure 2. Raindrop size distributions for a rainwater content of 1 g m^{-3} with the only difference in panels being the logarithmic *y* axis in the bottom panel. The solid black line represents a one-moment constant N_0 and $\mu = 0$ distribution as assumed in DHARMA-B, DHARMA-S, MESONH-1, and MESONH-2. The dashed black line represents a one-moment $\mu = 2.5$ distribution as assumed in UKMO-1 and UKMO-2. The solid gray lines represent the range of possible distributions in the $\mu = 0$ two-moment schemes used in DHARMA-2 M, SAM-B, SAM-S, and UKMO-2 M.

simulations include the Rapid Radiative Transfer Model longwave radiation scheme [*Mlawer et al*., 1997], the Dudhia shortwave radiation scheme [*Dudhia*, 1989], a five-layer thermal diffusion land surface scheme, and the Yonsei University planetary boundary layer scheme [*Hong et al*., 2006] for treating vertical turbulent mixing. Additional parameterizations used are comparable to those used in the CRM simulations, including a Smagorinsky-type first-order turbulence closure for treating horizontal turbulent mixing, Monin-Obukhov similarity theory for surface fluxes, fifth-order horizontal with third-order vertical advection of momentum and scalars, and positive definite moisture advection. In D1 and D2, the Kain-Fritsch convective parameterization [*Kain*, 2004] is used. A fourth simulation (WRF-M2) using WRF-ARW V3.3.1 that was not used in *Zhu et al*. [2012] also uses the Morrison microphysics scheme. This simulation uses almost the same setup as the three other WRF runs, except that cloud water *N* is set to 100 cm^{-3} rather than 250 cm^{-3} and ECMWF analysis nudging is turned off in D3 and the boundary layer of all domains. Microphysics schemes are not tuned for tropical maritime convection for any CRM and LAM simulations. For most comparisons to observations, WRF output with 10 min output frequency covering the same 33 h period as the CRM simulations that is within innermost domain (D4) is included. The LAM simulations were allowed 15 h to spin up.

2.3. Hydrometeor Size Distribution Parameters

Many results in this study make reference to hydrometeor size distribution parameters in bulk microphysics schemes. Most schemes assume gamma size distributions of the form $n(D) = N_0 D^{\mu} e^{-\lambda D}$ for precipitation-sized hydrometeors, where N_0 is the size intercept, μ is the shape parameter, and λ is the slope parameter. One exception is the snow scheme [*Grabowski*, 1999] used in DHARMA-B and DHARMA-S that uses a combined cloud ice and snow category characterized by a bimodal distribution. Another is the snow size distribution in the Thompson scheme characterized by a combination of two gamma size distributions. For a given water content, a higher N_0 yields a greater number of small particles, a higher μ yields a narrower size distribution, and a higher λ yields a faster decrease in number concentration with increasing particle size. Figure 2 shows the effects of N_0 and μ on the rain size distribution for 1 g m^{-3} rainwater content (RWC). Simulated Rayleigh reflectivity is calculated by integrating over the sixth moment of the melted equivalent diameter size distributions. For all ice species, a dielectric factor of 0.208/0.93 is used [*Smith*, 1984].

3. Observations

The primary observational tool used in this study is the C band (5.5-cm wavelength) scanning polarimetric precipitation radar known as CPOL [*Keenan et al*., 1998]. Because of distinct differences in dynamical and thermodynamical structure, it is useful to separate convective and stratiform regions. This is done using the

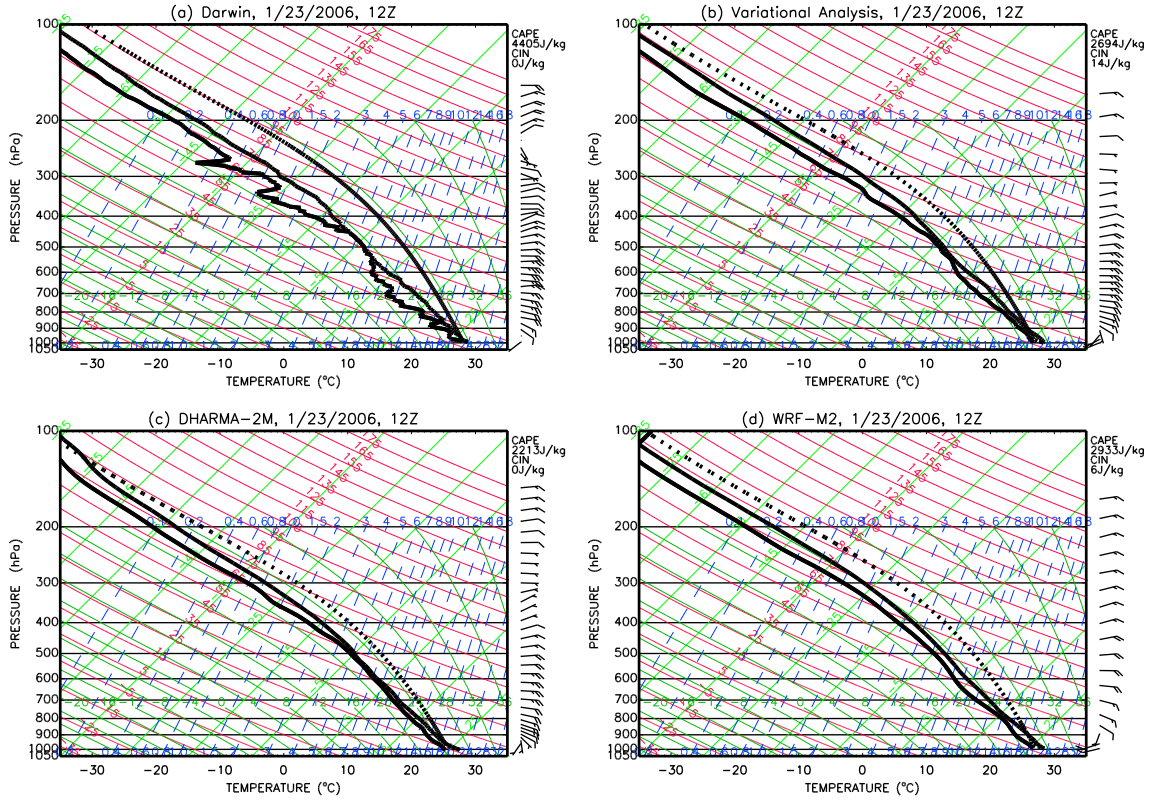

Figure 3. 12*Z* 23 January 2006 (a) Darwin observed, (b) variational analysis, (c) DHARMA-2 M domain mean, and (d) WRF-M2 domain mean soundings of temperature, dew point, and wind on skew *T* log *p* diagrams with undilute lifted surface parcel paths dotted (not including latent heat of fusion). Surface-based CAPE and convective inhibition are noted in the upper right of each panel.

Steiner et al. [1995] algorithm on 2.5-km horizontal resolution CPOL radar reflectivity at a 2.5-km altitude with a 5 dBZ lower bound on radar reflectivity to remove clutter. This algorithm was designed using Darwin radar data and works well for observed reflectivity. Simulated reflectivity can be biased high or low depending on assumed rain size distributions, which can therefore impact comparisons of observed and simulated convective and stratiform properties. However, without a well-founded better alternative, the same separation algorithm is applied for simulations and observations at the same horizontal resolution and altitude with sensitivity tests left for future studies. Further details can be found in *Varble et al.* [2011].

This study also uses dual-Doppler-retrieved 3-D wind fields described in *Collis et al.* [2013]. This retrieval uses radial velocity vectors from the operational Berrimah C band and research CPOL radars where the horizontal component of these vectors is between 30° and 150°. Shown in Figure 1a, this yields two lobes covering an area of 4165 km^2 that is approximately 7–8 times smaller than the CRM domain areas. Vertical wind speed is obtained in these lobes by integrating the anelastic continuity equation both upward from the surface and downward from echo top with a weighting function used in combining the two. The retrieval covers a 5 h period from 1310*Z* to 1750*Z* on 23 January 2006 during the peak of convective activity near the radars but before a squall line with trailing stratiform precipitation forms. Vertical velocity is assumed to be 0 at echo top, and convergence is assumed to be constant below the lowest radar beam down to the surface if a valid radar return at the lowest elevation angle is detected in that column. These are two sources of error because convergence may often increase toward the surface, as is seen in simulations, and some divergence may occur above the radar echo top, as discussed in *Mapes and Houze* [1995]. Assumed hydrometeor fall speeds are used with the vertical component of the radial velocity vectors as a weak constraint on the analysis. Due to smoothing, the true resolution of the analysis is likely at least 2–3 km despite output on 1-km grids. *Collis et al.* [2013] show that retrieved vertical velocities are comparable to higher-resolution vertical profiler *w* retrievals in several convective updrafts, yielding a root-mean-square error (RMSE) of 1.9 m s^{-1} and a negative bias in the dual-Doppler retrieval of 2.2 m s^{-1}.

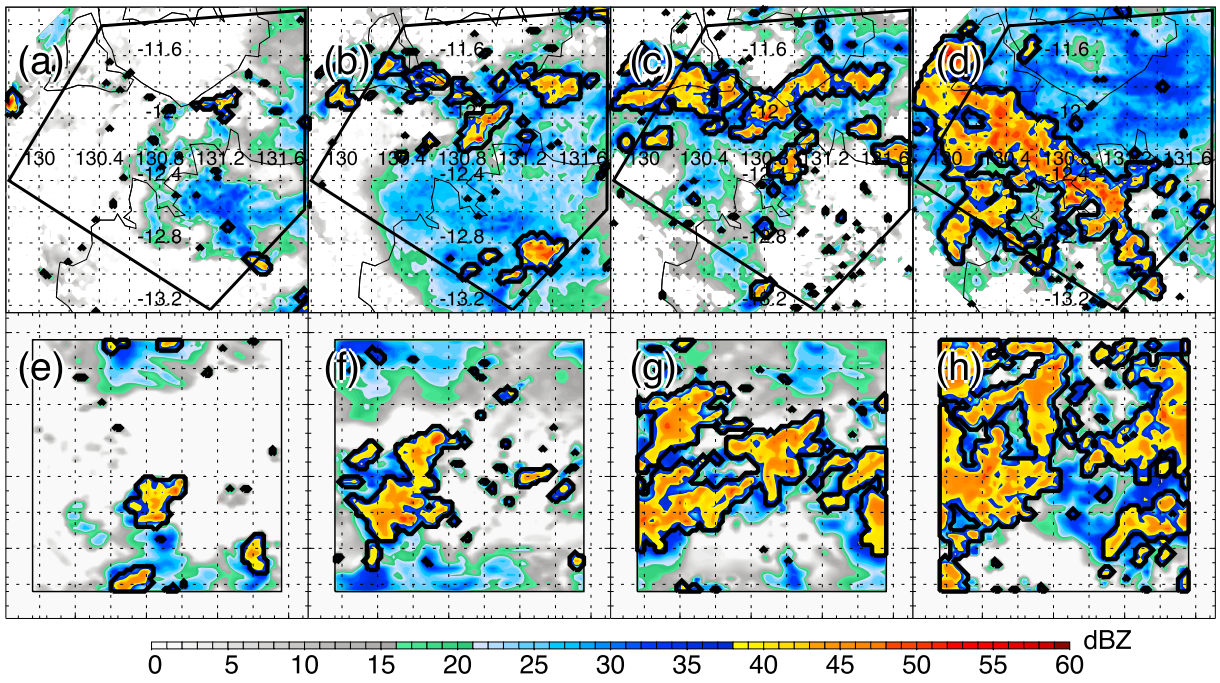

Figure 4. The 2.5 km altitude horizontal plan views of CPOL reflectivity at (a) 12*Z*, (b) 14*Z*, (c) 16*Z*, and (d) 18*Z* on 23 January 2006 and DHARMA-2 M reflectivity at the same times: (e) 12*Z*, (f) 14*Z*, (g) 16*Z*, and (h) 18*Z* on 23 January 2006. Convective regions are outlined in black. The pentagon in Figures 4a–4d is the region used to force the CRMs.

4. Results

4.1. Large-Scale Environment

The observed 12*Z* sounding on 23 January 2006 from Darwin in Figure 3a shows an environment with cloud bases of a few hundred meters and high relative humidity throughout the troposphere with substantial convective available potential energy (CAPE) and moderate vertical wind shear between 0 and 3 km, which is more typical of break period continental squall line scenarios [*Keenan and Carbone*, 1992]. The 3-hourly sounding sites represented by triangles in Figure 1a (not shown) produce soundings with similar characteristics to the 12*Z* Darwin sounding, although instability and vertical wind shear generally increase from east to west and the surface-based CAPE in the 12*Z* Darwin sounding shown is anomalously large relative to other soundings. The 12*Z* variational analysis sounding in Figure 3b has similar characteristics to the observed soundings, and therefore, it is not surprising that domain mean soundings from simulations, DHARMA-2 M in Figure 3c and WRF-M2 in Figure 3d, are also similar. Weaker midlevel and stronger upper level winds in WRF-M2 are a result of ECMWF analysis errors, while cooler temperatures in DHARMA-2 M are a result of accumulated radiative flux divergence since the start of the simulation at 0*Z* on 18 January 2006 [*Fridlind et al.*, 2012]. Other than these differences, values of CAPE greater than 2000 J kg^{-1}, vertical wind shear through 3 and 6 km depths of 10–15 m s^{-1}, veering of winds from surface westerly to southerly to easterly at 1.5-km altitude, and a bulk Richardson number of 35–40 are present in all observed and modeled soundings, and therefore simulated and observed domain mean large-scale environments are quite similar.

4.2. MCS Evolution

Animations of 2.5-km altitude reflectivity horizontal plan views from CPOL and all simulations from 3*Z* on 23 January to 12*Z* on 24 January 2006 can be found online as supporting information. Figure 4 shows CPOL and DHARMA-2 M 2.5-km altitude reflectivity with convective regions outlined in black at 12Z, 14Z, 16Z, and 18*Z* on 23 January 2006. These snapshots envelope the dual-Doppler observation period, which extends from 1310*Z* to 1750*Z* and will be the focus in this part of the manuscript. During this period, convection evolves from being isolated in nature to slightly more organized along boundaries to very organized along a northwest to southeast oriented line. Observed weak-moderate stratiform precipitation exists throughout

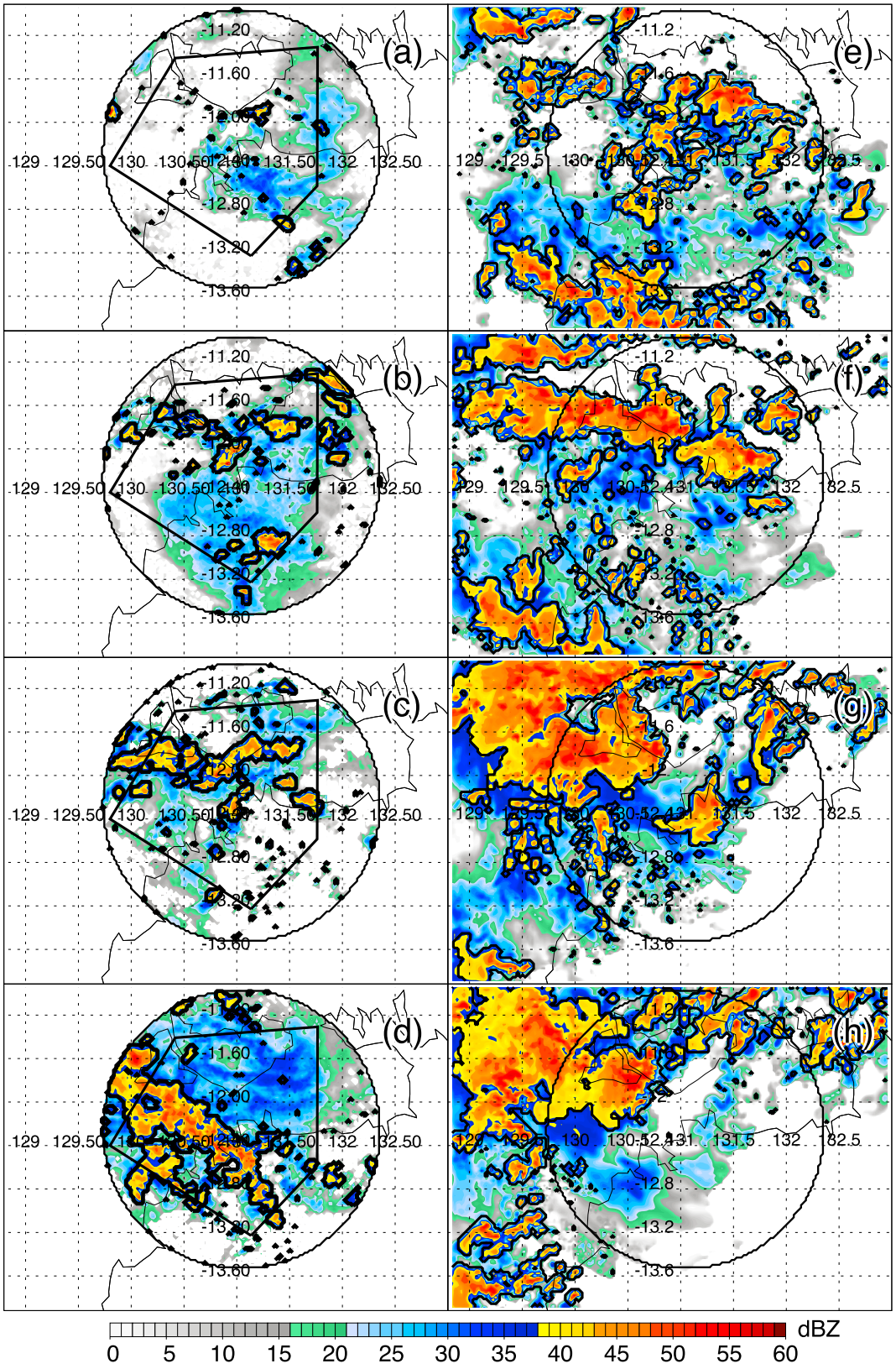

Figure 5. The 2.5 km altitude horizontal plan views of CPOL reflectivity at (a) 12*Z*, (b) 14*Z*, (c) 16*Z*, and (d) 18*Z* on 23 January 2006 and WRF-M2 reflectivity at the same times: (e) 12*Z*, (f) 14*Z*, (g) 16*Z*, and (h) 18*Z* on 23 January 2006. Convective regions are outlined in black. The pentagon in Figures 5a–5d is the region used to force the CRMs and the circle in all panels shows the extent of CPOL coverage.

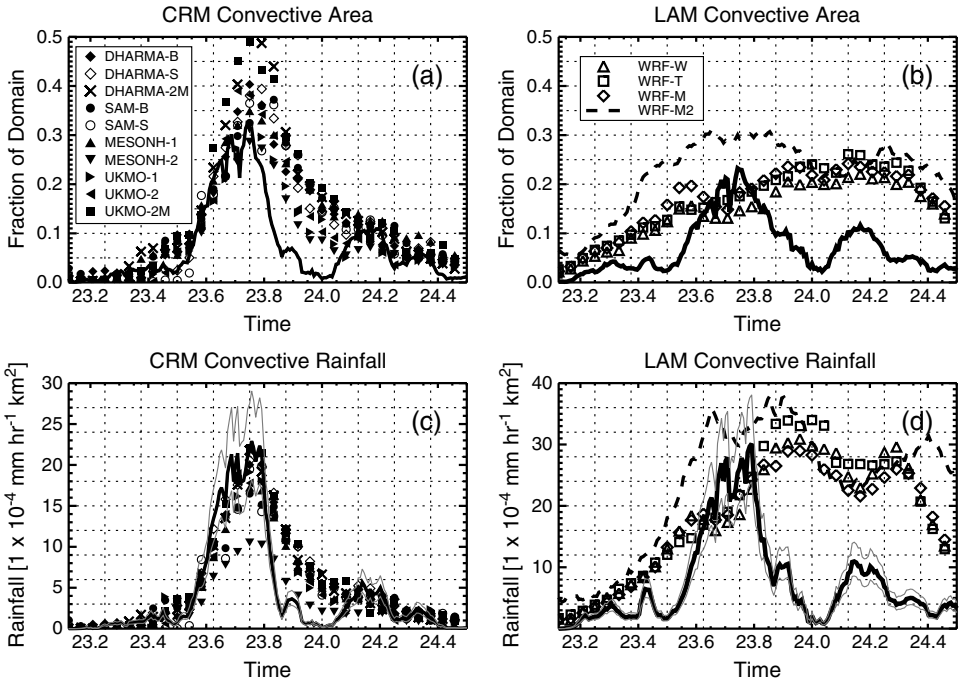

Figure 6. The time series of (a) CRM and (b) LAM convective area and (c) CRM and (d) LAM convective rainfall for the period from 3*Z* on 23 January to 12*Z* on 24 January 2006. Symbols and the dashed black lines represent simulations. Full inner domain LAM statistics normalized to the CPOL domain size are shown. Thick black lines depict CPOL observations limited to the pentagonal CRM forcing domain in Figures 5a and 5c and full domain in Figures 6b and 6d with uncertainty shown with gray lines in Figures 6c and 6d. Rainfall has units of 1×10^{-4} mm h^{-1} km^2.

this period, with more extensive and intense stratiform precipitation developing after an observed intense convective blowup around 17*Z* (as seen in the Animations S1 and S2 in the supporting information). DHARMA-2 M and other CRM simulations reproduce the transition from isolated convective cells to convection organized in squalls between 12 and 18*Z*. Figure 5 shows that the timing and positioning of convection is incorrect in WRF-M2 between 12 and 18*Z*, although the LAM simulations also represent a transition from scattered to more organized squall line convection between 10 and 14*Z* and again from 16 to 20*Z*, as seen in Animations S1 and S2 in the supporting information. There are also very clear negative aspects of the MCS evolution in simulations. For example, Figures 4 and 5 as well as Animations S1 and S2 show that all simulations clearly have a high bias in convective area during this period.

The observed squall line holds together from 18*Z* to approximately 21*Z* while propagating westward out of the CPOL domain and leaving a large stratiform precipitation in its wake, as shown in Animations S1 and S2 and Figures 2 and 3 of Part 2. The animations show that both the CRM and LAM simulations produce squall structures but struggle to develop a large stratiform precipitation region during the mature and decaying stages of the event (18*Z* onward), which is discussed more in Part 2.

4.3. Biases in Convective Area and Radar Reflectivity Aloft

Varble et al. [2011] showed that most CRM simulations using approximately 1-km horizontal grid spacing with different bulk microphysics representations overestimated convective area and radar reflectivity above the freezing level for the 6 day active monsoon period of TWP-ICE. Figure 6 shows the time series of CRM and LAM convective area and rainfall for the MCS event. Both CRMs and LAMs generally overestimate convective area and rainfall. CRM simulations fairly accurately reproduce the time series of rainfall in Figure 6c because rainfall is an input to their forcing with a slower decline in convective precipitation likely resulting from periodic boundary conditions. LAM simulations also have a peak in convective rainfall in Figure 6d, but it is much broader. This is partially a result of their larger domain that captures convection over a longer period of time but primarily a result of overactive and slow-moving convection shown in Animations S1 and S2 and Figures 3 and 4.

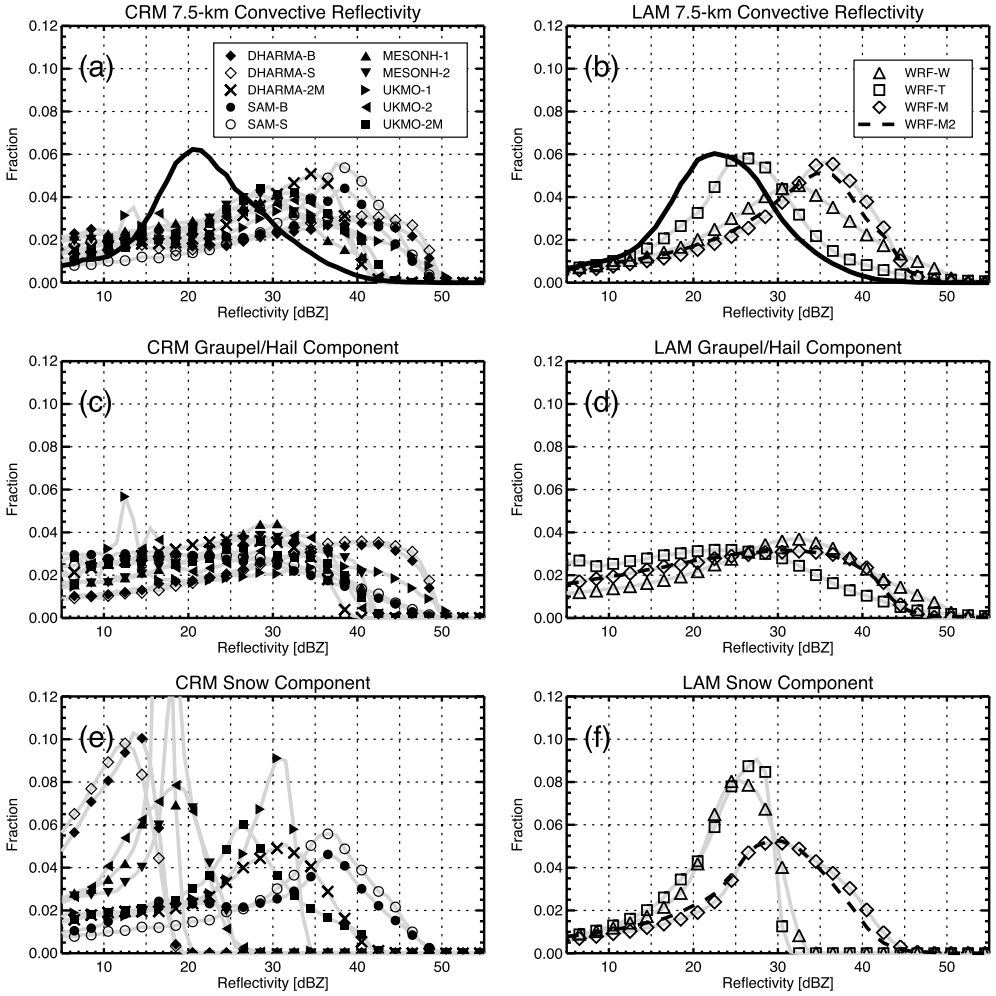

Figure 7. Probability distributions of 7.5 km altitude (a) CRM- and (b) LAM-simulated convective radar reflectivity, (c) CRM- and (d) LAM-simulated graupel radar reflectivity, and (e) CRM- and (f) LAM-simulated snow reflectivity. Gray lines with symbols and dashed black lines represent simulations, and the thick black line represents CPOL observations limited to the pentagonal CRM forcing domain in Figure 7a and full domain in Figure 7b.

In agreement with *Varble et al*. [2011], Figure 7a shows that CRM simulations overestimate 7.5-km altitude convective reflectivity, while Figure 7b shows that LAM simulations also overestimate reflectivity above the freezing level. While Figures 7c and 7d show that graupel is a major source of the high bias in radar reflectivity, Figures 7e and 7f show that snow is also a major contributor in the two-moment Morrison scheme used in CRM simulations (SAM-B, SAM-S, UKMO-2 M, and DHARMA-2 M) and LAM simulations (WRF-M and WRF-M2). There is a clear separation of LAM snow radar reflectivity values in one-moment (WRF-W, WRF-T) and two-moment (WRF-M, WRF-M2) microphysics schemes in Figure 7f. The unique snow scheme in WRF-T produces results closest to observations. It assumes that snow mass is proportional to D^2 rather than D^3, which is assumed in other schemes, and it diagnoses moments of the snow size distribution as a function of temperature based on *Field et al*. [2005]. This allows snow density to decrease with increasing size, which is more observationally based [*Locatelli and Hobbs*, 1974; *Field et al*., 2005]. Without variable N_0, however, snow radar reflectivity would likely be biased low in WRF-T as it is in MESONH in Figure 7e, which assumes snow mass proportional to $D^{1.9}$. Because two-moment schemes already allow for a variable N_0, a two-moment scheme assuming snow mass proportional to $D^{1.9}$ or D^2 rather than D^3 would likely produce reflectivities closer to those observed. Unlike snow, graupel contributes to a high bias in radar reflectivity in all simulations, which is a well-known problem in bulk microphysics schemes used in CRM and LAM simulations of deep convective systems around the world. *Lang et al*. [2011] adjusted graupel and snow microphysical processes in a bulk scheme within tropical deep convective simulations to partially alleviate this problem, but doing so

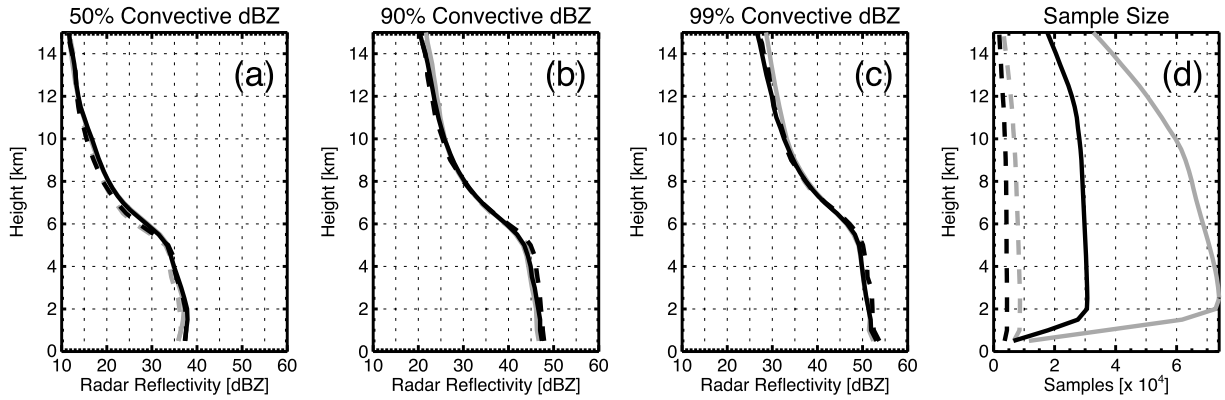

Figure 8. The (a) 50th, (b) 90th, and (c) 99th percentiles of convective radar reflectivity and (d) sample size in the dual-Doppler lobes (dashed lines) and pentagonal model forcing domain (solid lines). Gray lines represent statistics for the entire MCS event, while black lines represent statistics for the 1310*Z* through 1750*Z* dual-Doppler observing period on 23 January 2006.

assumes that ice size or category is the driver of the high bias. However, as discussed further below, ice mass aloft may be as significant as ice size or category, and if it is, convective updraft dynamics may also be a contributor to the high bias in radar reflectivity aloft.

4.4. Observed and Simulated Deep Convective Updraft Radar Reflectivity and Vertical Velocity

For simulations and dual-Doppler retrievals, convective updrafts are defined three dimensionally in space by connecting all contiguous points at which w is greater than or equal to 1 m s^{-1} with no reflectivity requirement. Because uncertainty in dual-Doppler retrievals is a few m s^{-1} [*Collis et al.*, 2013], comparisons between models and such retrievals are reserved for cores of large updrafts. These *deep updrafts* are defined here as those that begin below 1-km and end above 15-km altitude (the tropopause is located at approximately 17 km). Dual-Doppler and simulated updrafts that meet this definition account for ~75–90% of

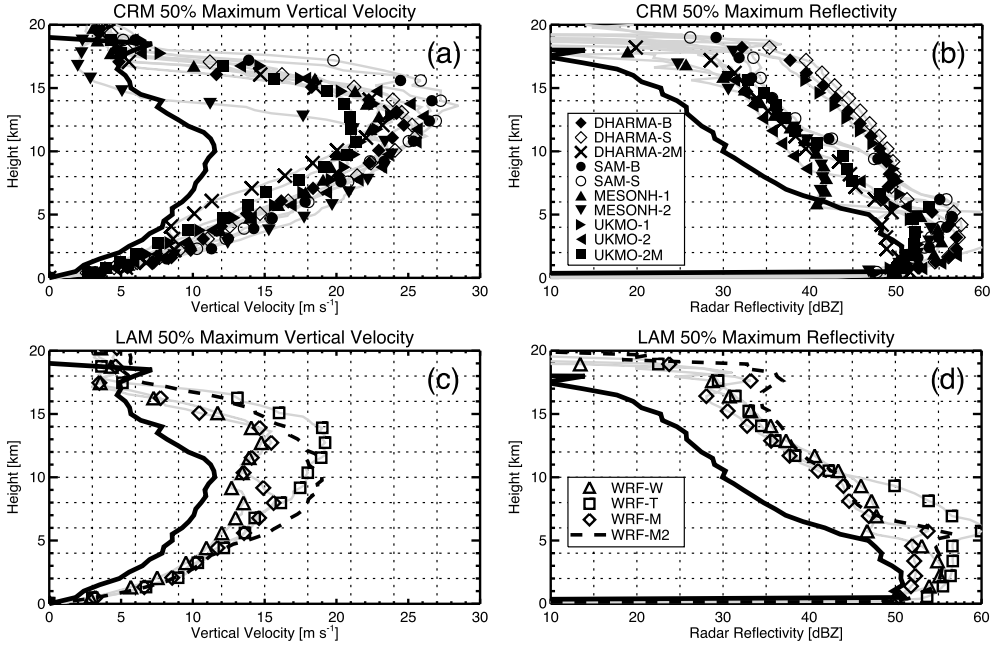

Figure 9. Median profiles of maximum (a, c) vertical velocity and (b, d) radar reflectivity for three dimensionally defined convective updrafts beginning below 1 km and ending above 15 km for the period of 1310*Z* to 1750*Z* on 23 January 2006. CRM statistics are shown in Figures 9a and 9b and LAM statistics are shown in Figures 9c and 9d. Gray lines with symbols and the dashed black lines represent simulations. Observations are represented by solid black lines.

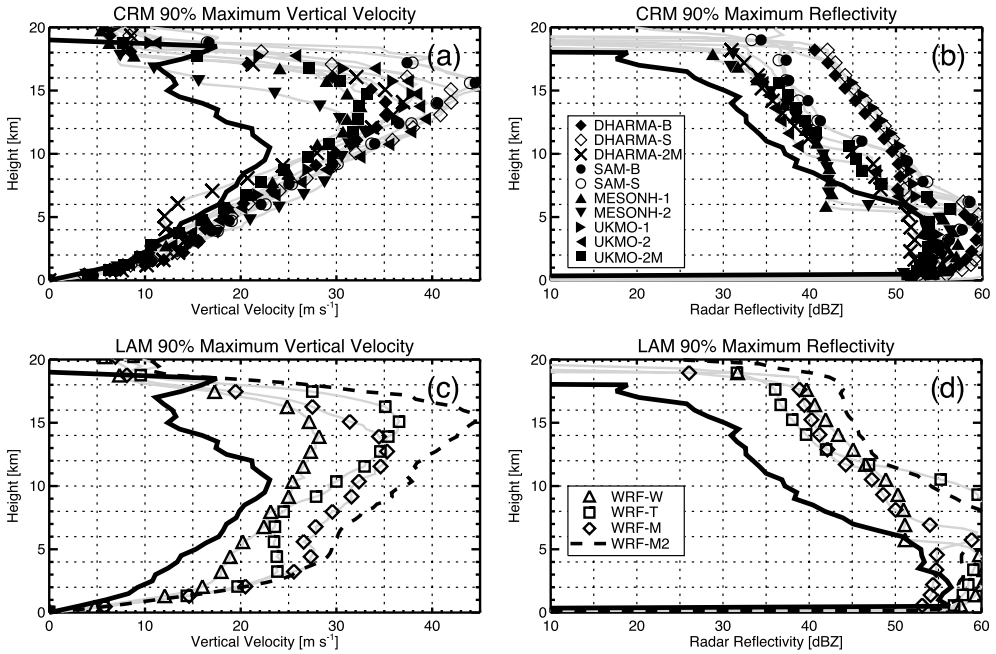

Figure 10. The 90th percentile profiles of (a) CRM-simulated maximum vertical velocity, (b) CRM-simulated maximum radar reflectivity, (c) LAM-simulated maximum vertical velocity, and (d) LAM-simulated maximum radar reflectivity for simulated and observed deep convective updrafts as in Figure 9. Gray lines with symbols and dashed black lines represent simulations. Observations are shown with the solid black line.

the total updraft mass flux at middle and upper levels for the 1310*Z* through 1750*Z* dual-Doppler retrieval period during the peak of the event near Darwin. Comparisons are made for this retrieval period using 10 min output, and these will be the focus for comparisons throughout the rest of this paper. Using radar reflectivity aloft as a convective intensity proxy [*Zipser and Lutz*, 1994], Figure 8 shows that the 50th, 90th, and 99th percentile profiles of observed CPOL convective radar reflectivity (as defined using the *Steiner et al*. [1995] algorithm) in the dual-Doppler lobes are very similar to profiles in the pentagonal model forcing domain for both the 5 h dual-Doppler retrieval period and the entire MCS event. This indicates that the dual-Doppler sampling is representative of both the CRM model forcing domain and the MCS event.

The 50th percentiles of retrieved, CRM-simulated, and LAM-simulated deep updraft maximum *w* and maximum radar reflectivity as a function of height are compared in Figure 9 for an observed sample size of 60, CRM sample sizes ranging from 65 to 190, and LAM sample sizes exceeding 200 deep updrafts in all simulations. In this comparison and comparisons in Figure 10, a 1-km horizontal mesh available for the dual-Doppler lobes is used rather than the 2.5-km mesh used in *Varble et al*. [2011] and Figures 4–8 that is available for the entire CPOL domain. There is a clear separation of dual-Doppler retrieved *w* represented by the black line and simulated *w* represented by symbols (Figures 9a and 9c). At the freezing level (~4.7-km to ~5.5-km altitude in the updrafts), simulations show a range of maximum *w* values between 10 and 17 m s^{-1}, which are faster than almost all simulated rain mass-weighted fall speeds, meaning any raindrops in these updraft cores are lifted above the freezing level if not advected out of the core. Dual-Doppler retrievals, however, show maximum *w* values at the freezing level of approximately 8 m s^{-1}. Taking the ~2 m s^{-1} dual-Doppler retrieval negative bias reported by *Collis et al*. [2013] into account yields a 10 m s^{-1} maximum *w* value, similar to values in the DHARMA-2 M and WRF-W simulations but still less than other simulations. Maximum *w* differences are larger in the upper troposphere where CRM-simulated values peak between 21 and 28 m s^{-1} in Figure 9a, but dual-Doppler retrieved values peak at slightly less than 12 m s^{-1}. Adding the dual-Doppler retrieval RMSE and bias given by *Collis et al*. [2013] only yields 4 m s^{-1}, so much of these differences are very likely real. LAM-simulated maximum *w* values peak between 15 and 20 m s^{-1} aloft in Figure 9c, which is less than the values in CRMs but still greater than the dual-Doppler retrievals aloft. Deep updraft average *w* is also lesser in LAMs than in CRMs, although still greater than dual-Doppler retrieved values (not shown). As shown in the Figure 6 time series, WRF-M2 exhibits a double peak in convective precipitation

and the other LAM simulations exhibit a near-constant large amount of convective precipitation between 12*Z* on 23 January and 6*Z* on 24 January 2006, which differs from the single peak in observations and CRM simulations. Thus, some of the difference between LAMs, CRMs, and observations may be related to differences in location and timing of the MCS event related to differences in large-scale forcing.

The largest separation between simulated and observed maximum radar reflectivity in Figures 9b and 9d is above the freezing level, especially above 8 km. The median of maximum reflectivity at 10 km is 30 dBZ in observations but ranges from 37 to 49 dBZ in simulations. As was the case for maximum *w*, the median value of maximum reflectivity at 5 km in DHARMA-2 M and dual-Doppler retrieved updrafts matches, but other simulations yield greater maximum reflectivities at this height. Potential reasons for these differences are discussed in the next section. The very large reflectivities in WRF-T between 5 and 8 km in Figure 9d are a result of very large graupel particles with high mass fall speeds, resulting from low values of N_0, which is diagnostically calculated as $\frac{200}{q_g}\mathrm{m}^{-4}$ (q_g is dimensionless mass mixing ratio) with a lower bound of $1\times10^4\,\mathrm{m}^{-4}$. This is also discussed further in the next section. Most simulations show increasing average reflectivity (not shown) and constant maximum reflectivity with increasing height below the freezing level, whereas observations show decreasing average and maximum reflectivity with height. This may be a function of large raindrops falling out of observed deep updrafts but not out of simulated deep updrafts, which lends credence to low- and middle-level updrafts being stronger in simulations than in observations. Despite similar *w* profiles in all simulations, there is considerable spread in radar reflectivity aloft, which is a result of different assumptions in defining hydrometeor properties, as discussed in *Varble et al*. [2011].

The 90th percentile of simulated deep updraft properties in Figure 10 yields a different result than the 50th percentile properties in Figure 9. Retrieved and CRM-simulated 90th percentile maximum *w* values between the surface and 10 km are similar (Figure 10a), ranging from 15 to 20 m s^{-1} at the freezing level. Above 10 km, however, the dual-Doppler retrieval and simulations diverge with simulations showing substantially stronger updrafts. In all but the WRF-W simulation, LAM-simulated maximum *w* exceeds 20 m s^{-1} below the freezing level in Figure 10c, stronger than in the CRMs. In the upper troposphere, all but the WRF-W simulation have peak *w* values between 34 and 40 m s^{-1}, which fall within the distribution of CRM values. A possible reason for lesser *w* in WRF-W is that it has a much drier upper troposphere than in other simulations, as discussed more in Part 2 of this study. This finding may seem to contradict *Wu et al*. [2009] and *Van Weverberg et al*. [2013]; however, they use different time periods, domain sizes, model resolutions, convective updraft definitions, and examination methods (e.g., mean versus maximum quantities). Despite the WRF-W outlier, it is clear that similar biases exist in the CRMs and LAMs, although greater variability exists in the LAMs, possibly related to less constraint in the LAM large-scale forcing.

The observed 90th percentile of maximum reflectivity at 10 km is 37 dBZ, while simulated values range from 40 to 57 dBZ in Figures 10b and 10d. The observed 90th percentile profile of maximum reflectivity decreases with height between 2 and 5 km consistent with the 50th percentile profile and the rate at which observed maximum reflectivities decrease aloft is similar to rates in simulations using two-moment schemes. As was the case for the 50th percentile, significant spread in simulated radar reflectivity aloft exists between 5 and 10 km despite a small spread in updraft *w*. Microphysics schemes that can offset large ice water contents (IWCs) by increasing *N*, whether through its prediction in a two-moment scheme or diagnostically varying N_0 in a one-moment scheme, generally produce deep updraft maximum reflectivities closest to observed. High snow and graupel N_0 values and nonspherical *m-D* relationships assumed in the MESONH one-moment scheme produce the lowest reflectivities between 6 and 9 km in Figure 10b, although MESONH reflectivity does not decrease as quickly with height as observed, a property common to one-moment schemes with constant N_0 values.

In situ aircraft measurements of maximum updraft *w* in other studies support the dual-Doppler retrieved values for this case. Values reaching 15 m s^{-1} at ~6-km altitude have been measured by aircraft in a strongly forced tropical depression [*Zipser and Gautier*, 1978] and oceanic MCS case [*Jorgensen and LeMone*, 1989] with updrafts that are ~10 km wide or greater when spatial resolution is degraded to 1 km. While tropical monsoonal convection is often more intense than convection over the open ocean [*Petersen and Rutledge*, 2001; *Xu and Zipser*, 2012] and this MCS case is comparable to strongly forced oceanic tropical depression systems in *Zipser and Gautier* [1978] and *Houze et al*. [2009], it is still weaker than typical break period continental convection [*May and Ballinger*, 2007; *Xu and Zipser*, 2012] for which reflectivities greater than

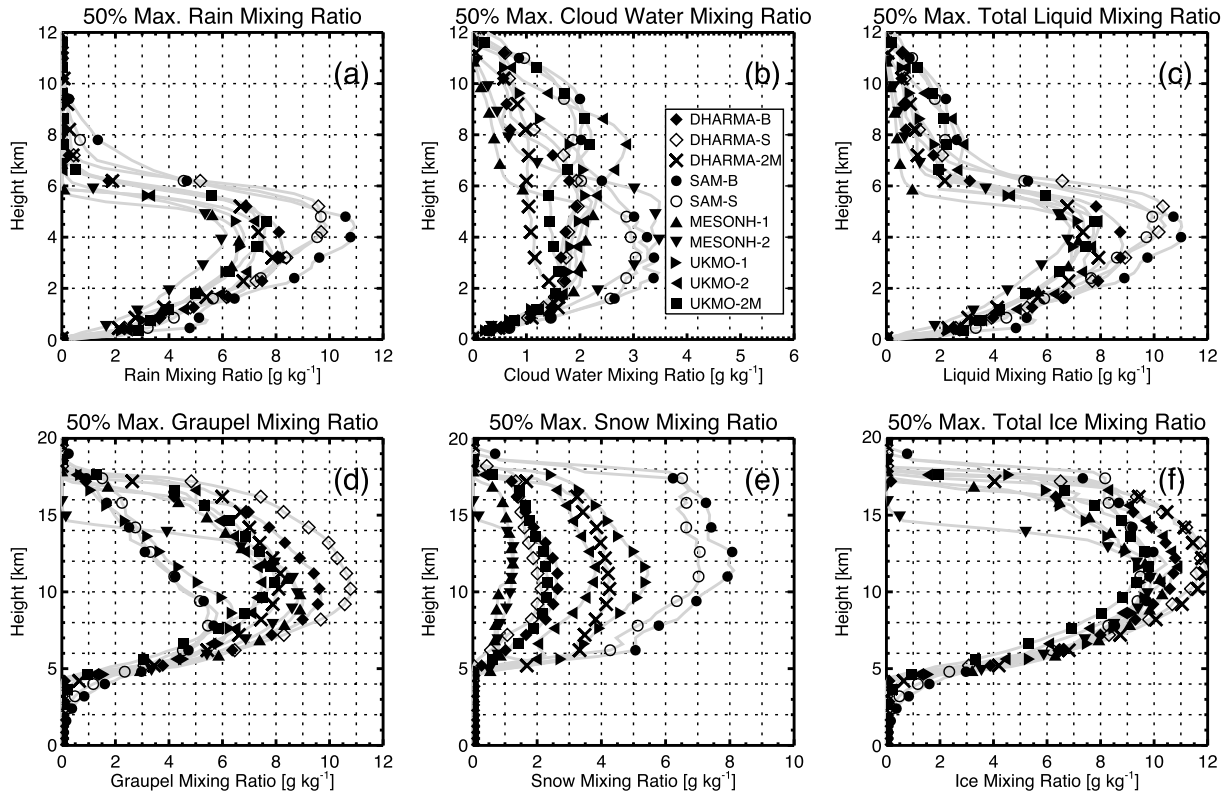

Figure 11. The 50th percentile of CRM-simulated maximum (a) rain, (b) cloud water, (c) total liquid, (d) graupel/hail, (e) snow, and (f) total ice (graupel/hail, snow, and cloud ice) mixing ratios in deep convective updrafts as in Figure 9.

40 dBZ are common above 10-km altitude and *Simpson et al.* [1993] inferred peak upper tropospheric *w* values are greater than 30 m s^{-1}.

Heymsfield et al. [2010] report mean oceanic peak *w* values of 10 m s^{-1} at 5-km altitude and 13 m s^{-1} at 10-km altitude with peak *w* values occurring between 10 and 12-km altitude. These values are similar to median dual-Doppler statistics in Figure 9, but simulated peak *w* values are larger and occur at higher altitudes. The peak oceanic *w* in *Heymsfield et al.* [2010] at 5 km is 17 m s^{-1} and 25 m s^{-1} at 10 km, which are very close to the dual-Doppler 90th percentile peak *w* values of 15 m s^{-1} at 5 km and 23 m s^{-1} at 10 km in Figure 10 and the 20 m s^{-1} peak *w* at 11 km reported in *Lawson et al.* [2010] for an intense updraft off of the Central American coast. *Heymsfield et al.* [2010] also show that the mean of the maximum radar reflectivity in their oceanic cells is 30 dBZ at 10 km with maximum values nearing 40 dBZ, which agrees with the dual-Doppler retrievals in Figures 9 and 10, but is significantly lesser than the simulated values. In addition to scanning radar and vertical velocity observations, observations of hydrometeor properties in convective updrafts as a function of temperature are also needed. Unfortunately, bulk condensate mass observations in regions of large water content (e.g., greater than 1 g m^{-3}) have large uncertainties for most previous field campaigns, which means that comparisons are limited to condensate properties in different simulations.

4.5. Simulated Deep Convective Updraft Condensate

Figure 11 shows substantial differences between simulated hydrometeor mass mixing ratios as a function of hydrometeor type based on the microphysics scheme used. Cloud water, for example, strongly depends on whether *N* is predicted. DHARMA-2 M is significantly different from other two-moment cloud water schemes that do not include consumption of aerosols (Figure 11b). It produces the least cloud water with a ~1 g kg^{-1} median value of maximum cloud water mass mixing ratio at midlevels, whereas the SAM simulations that use a two-moment cloud water scheme have values near 3 g kg^{-1}, the greatest of all simulations. There are also

substantial differences between one-moment schemes that use a constant cloud water N and two-moment cloud water schemes that do not. For average cloud water mass mixing ratios (not shown), all two-moment schemes have less cloud water than all one-moment schemes except in the upper troposphere, where significant cloud water mixing ratios exist up to the homogeneous freezing level. This may further indicate that simulated updrafts are too strong, although deep convection observed in this case is likely stronger than that observed in other tropical oceanic field campaigns that show very little cloud water at temperatures colder than −20°C [*Stith et al*., 2004, 2006; *Heymsfield et al*., 2009]. For example, *Lawson et al*. [2010] suggest that homogeneous freezing of cloud water was a source for ice particles at 11 km ($T = -47$°C) in an oceanic, near-coastal convective turret with a vertical wind speed of 20 m s^{-1}.

Biases produced by precipitation-sized hydrometeors are more affected by size distribution assumptions than by representation of cloud water, with an exception being the effect of the cloud droplet nucleation scheme on rain in DHARMA-2 M. Aerosols and cloud water are consumed efficiently at low levels in DHARMA-2 M deep convective updrafts. With minimal mixing of ambient air into the strongest updraft cores, this leads to very high supersaturations, which limits condensational heating and lessens updraft maximum reflectivity between 2 and 5 km and maximum w between 3 and 9 km in Figures 9 and 10 relative to simulations without aerosol consumption. The SAM simulations, unique in their use of hail rather than graupel, have the smallest rimed ice mixing ratios (Figure 11d) and greatest snow-mixing ratios (Figure 11e) in the upper troposphere, which is consistent with results in several other studies [*Gilmore et al*., 2004; *van den Heever and Cotton*, 2004; *Morrison and Milbrandt*, 2011; *Van Weverberg et al*., 2012]. Hail mass-weighted fall speeds are often greater than twice those of graupel in the Morrison scheme, allowing faster sedimentation out of the updraft. The slow mass-weighted fall speeds of graupel (2–4 m s^{-1}) and snow (~1 m s^{-1}) allow large IWCs to be lofted into the upper troposphere in deep convective updrafts and advected over large areas, which produces larger than observed regions at a 2.5-km altitude of radar reflectivity with 40 dBZ or greater echoes identified as convective in the *Steiner et al*. [1995] algorithm. This can lead to median convective rain rates in some simulations that are less than those observed despite higher maximum convective rain rates [*Varble et al*., 2011] and stronger deep convective updrafts (Figures 9 and 10). Of the schemes using graupel rather than hail, the smallest graupel (Figure 11e) and highest snow (Figure 11f) mass mixing ratios are in the UKMO-1 and UKMO-2 simulations that assume $\mu = 2.5$ rather than 0. Of these two simulations, the two-moment UKMO-2 simulation produces more graupel and less snow than the one-moment UKMO-1 but produces convective radar reflectivity aloft much closer to observed in Figures 9 and 10 because prediction of N in UKMO-2 reduces graupel particle sizes.

Figure 11a shows that median values of CRM maximum rain mass mixing ratio peak between 5.5 and 10 g kg^{-1} just below the freezing level in all simulations, while the 90th percentile of maximum CRM condensate mass mixing ratios in Figure 12a are 9 to 15 g kg^{-1} around the freezing level (~5 km). This indicates that a significant portion of rain is not falling out of deep updraft cores before encountering temperatures of −4°C where raindrops begin freezing, which is consistent with constant or increasing radar reflectivity with height in simulated deep convective updrafts in Figures 9 and 10. Figure 11a shows that many large RWC values at 5-km altitude are colocated with w values stronger than 10 m s^{-1} in WRF-M2. In fact, any rain colocated with w values of 10 m s^{-1} or stronger moves upward (Figure 13b), and many large RWCs are being carried upward near the freezing level (Figure 13c). Although Figure 13 only shows WRF-M2 results, the last statement is true for all simulations, which produce similar results. This leads to very large ice mass mixing ratios aloft, peaking between 9.5 and 12 g kg^{-1} in the median profiles in Figures 11f and 13 to 14 g kg^{-1} in the 90th percentile profiles in Figure 12a. The largest values are produced in the sensitivity simulations (open symbols) in which the thermodynamic profiles are nudged toward the forcing state.

Figure 12b shows that the 90th percentile of condensate mass mixing ratios in WRF-W agree well with those in the CRM simulations shown in Figure 12a. WRF-M and WRF-M2 produce 90th percentile peak condensate mass mixing ratios of 14–16 g kg^{-1} at 5 km and 16–17 g kg^{-1} at 12 km, even larger than what the CRM simulations produce. Shown in Figure 14a, median values of maximum liquid mass mixing ratio vary from 6 to 9 g kg^{-1} in the LAM simulations and peak just below the freezing level, which is similar to the CRM results. Significant amounts of cloud water in all but the WRF-W run exist up to 8–10-km altitudes (Figure 14b), also similar to many of the CRM runs. Median values of maximum ice mass mixing ratio peak between 6 and 10 g kg^{-1} aloft (Figure 14f) and are lesser in the WRF-W and WRF-T runs than in any CRM simulation. For WRF-W, this is consistent with its lower w values in Figures 9 and 10 and thinner updrafts (not shown). WRF-T is the only

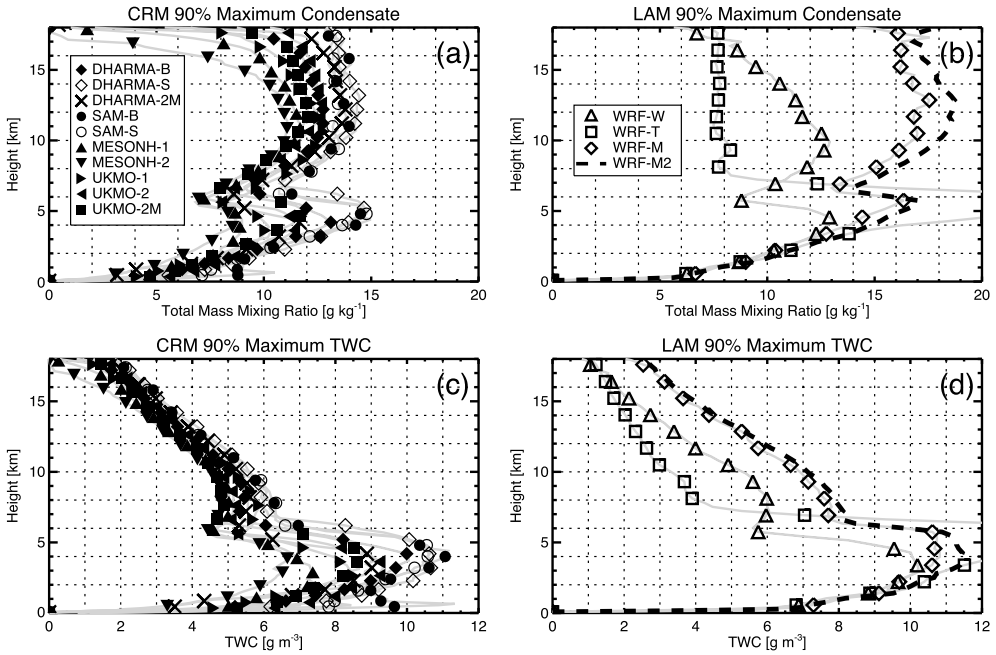

Figure 12. The 90th percentile profiles of maximum total hydrometeor mixing ratios in deep convective updrafts within (a) CRM simulations and (b) LAM simulations, and the 90th percentile profiles of maximum total hydrometeor water contents in deep convective updrafts as in Figure 9 within (c) CRM simulations and (d) LAM simulations.

simulation that does not have a relative minimum between 6 and 7 km produced by differing hydrometeor fall speeds. Graupel N_0 in WRF-T is diagnostically lessened to produce larger graupel particle sizes and fall speeds when prognostic graupel mass mixing ratios become larger. This causes a convergence of graupel mass at 5–6 km that further increases graupel particle sizes and fall speeds, preventing large graupel amounts from being lofted. This is shown clearly in Figure 12d. The 90th percentile of WRF-T simulated peak water content reaches 17 g m^{-3} between 4 and 6 km even though the *x* axis is limited to 12 g m^{-3}, while the 99th percentile astoundingly reaches 25 g m^{-3} with mass-weighted mean diameters exceeding 10 mm (not shown). The negative effect of these extremely large-condensate loadings on buoyancy are the likely cause of the decrease in the 90th percentile maximum *w* between 3 and 7 km in Figure 10 that does not appear in other simulations. Lesser upper tropospheric graupel in WRF-T (Figure 14d) leads to more snow production (Figure 14e), just as the use of hail in SAM CRM runs leads to more snow production (Figure 11e). Some of these differences between microphysics schemes are consistent with findings in *Wang et al.* [2009] and *Van Weverberg et al.* [2013].

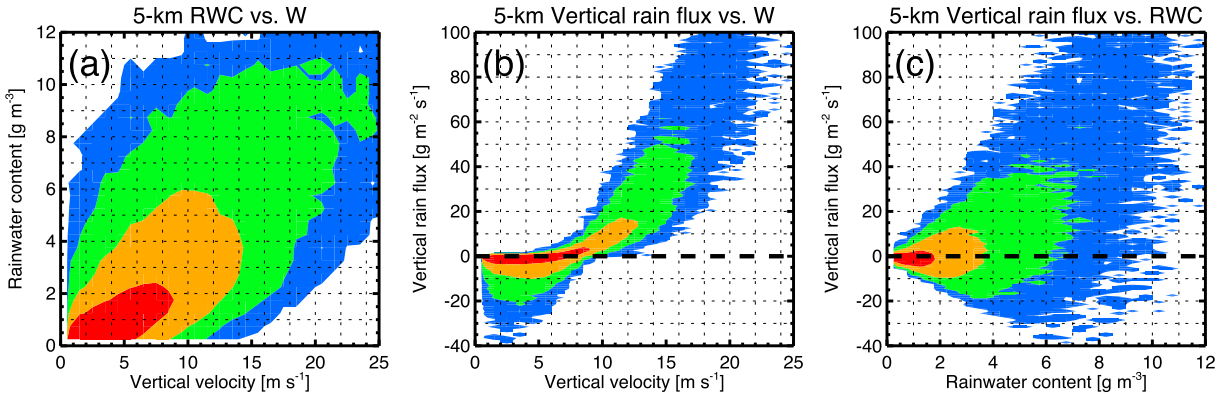

Figure 13. Joint histograms of 5 km altitude (a) rainwater content versus vertical velocity, (b) vertical rain flux versus vertical velocity, and (c) vertical rain flux versus rainwater content for WRF-M2 deep convective updrafts as in Figure 9. Vertical rain flux is defined as the rainwater content multiplied by the difference of the vertical velocity and the rain mass fall speed. All grid points within three dimensionally defined deep updrafts are included. Contour intervals are 1, 10, 100, and 1000.

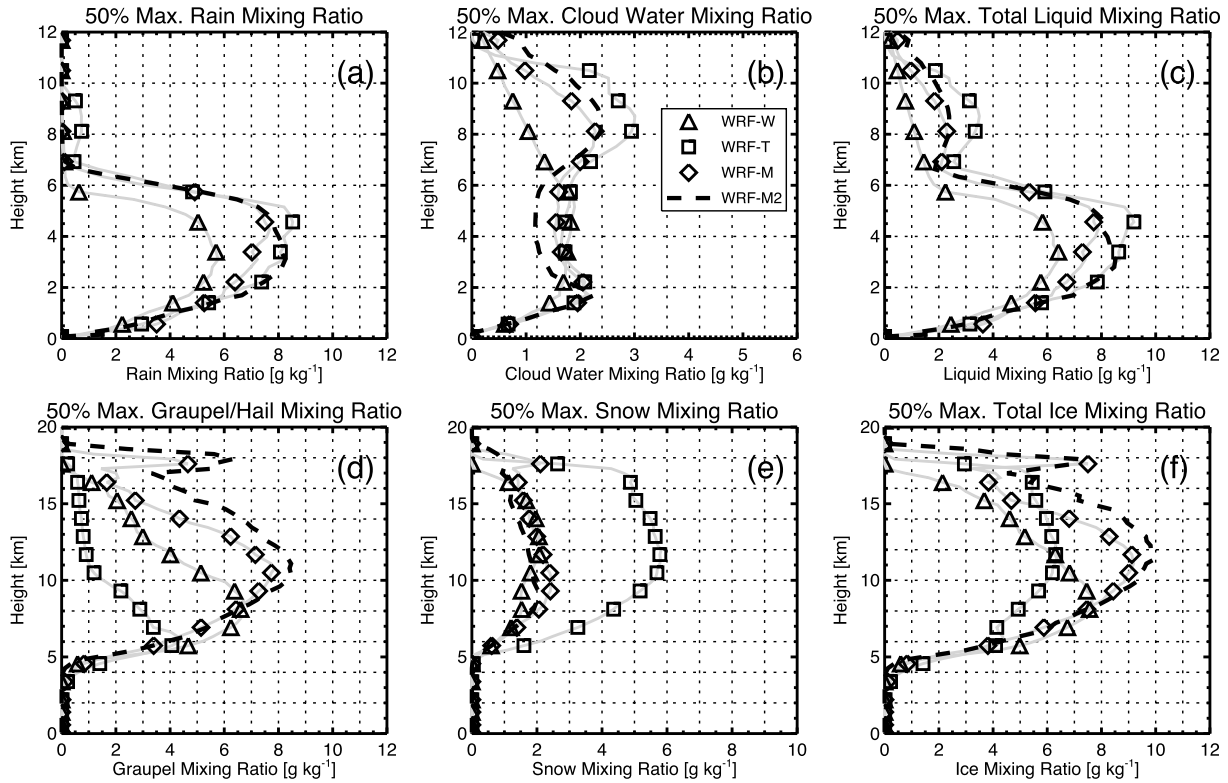

Figure 14. The 50th percentile of LAM-simulated maximum (a) rain, (b) cloud water, (c) total liquid, (d) graupel, (e) snow, and (f) total ice (graupel, snow, and cloud ice) mixing ratios in deep convective updrafts as in Figure 9.

WRF-W, having among the lowest median of maximum IWCs aloft, produces similar 90th percentile results to CRM simulations in Figure 12c that yield peak IWCs in the range from 4 to 5.5 g m^{-3} at 11-km altitude, about twice the estimated 2.4 g m^{-3} peak IWC in the convective turret described in *Lawson et al.* [2010] that had a peak w (20 m s^{-1}) similar to the 50th percentile simulated and 90th percentile dual-Doppler retrieved values in this TWP-ICE MCS case. An IWC of 2.4 g m^{-3} matches the median of 11-km altitude peak IWCs in WRF-W and WRF-T, but is still lower than the median of 11-km altitude peak IWCs in all other simulations that range from 3.5–4.3 g m^{-3} (not shown). WRF-M and WRF-M2 have the highest water contents aloft, 6 g m^{-3} at 11-km. At midlevels, CRM- and LAM-simulated 90th percentile maximum water contents peak at higher altitudes than in the 50th percentiles (not shown) with typical values of 7–11 g m^{-3}, showing that large RWCs are not efficiently falling out of the strongest updrafts. At 15-km altitude, the 90th percentile simulated peak IWCs are half of their values at ~10 km (Figures 12c and 12d), indicating fallout of ice mass in upper level updraft cores, but at a rate too slow to decrease water-loading effects on buoyancy because large mass mixing ratios shown in Figures 12a and 12b remain between 8 and 15 km. Although a large spread exists between different microphysics schemes, CRM and LAM deep updraft characteristics have the common issue of being overly intense with large condensate loadings, which raises the question of how such conditions are produced.

4.6. Production Mechanisms for Overly Strong Simulated Updrafts

Figure 15 shows four vertical cross sections through simulated strong deep convective updrafts in the four CRMs. Moist static energy (MSE), which is color filled, remains nearly constant between the surface and the freezing level in the updraft cores, which are signified by thick black w contours. This signifies minimal mixing of low MSE ambient air and high MSE air in updraft cores since MSE is approximately conserved for moist adiabatic ascent not involving freezing. MSE with temperature units is defined in equation (1):

$$\mathrm{MSE} = T + \frac{gz}{c_p} + 1 \times 10^6 (2.501 - 0.00237 T_c) \frac{q_v}{c_p}, \quad (1)$$

where T is absolute air temperature, g is gravity, z is height, c_p is the specific heat capacity of air at constant pressure, T_c is air temperature in Celsius, and q_v is specific humidity. Shown in Figure 16, the 50th to 90th

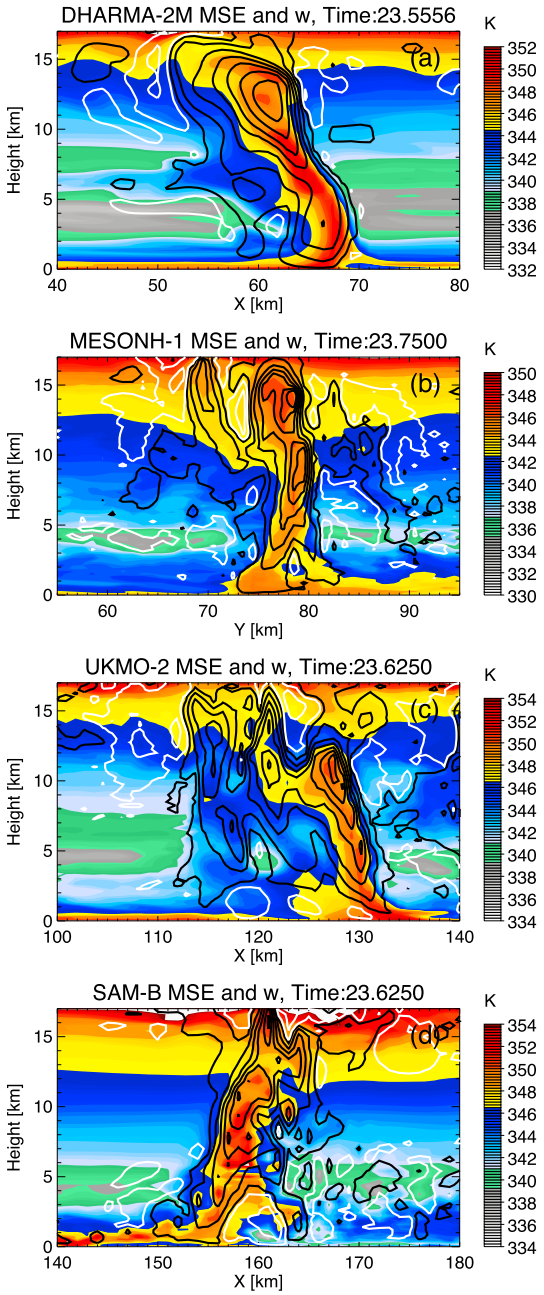

Figure 15. Example vertical cross sections through strong deep convective updrafts are shown for each of the CRM dynamical cores: (a) DHARMA, (b) MESONH, (c) UKMO, and (d) SAM. Moist static energy is filled. Upward vertical velocity is contoured in black at 1, 5, 10, 15, 20, 25, and 30 m s^{-1}, while downward vertical velocity is contoured in white at −1 and −5 m s^{-1}.

percentiles of maximum MSE decrease by 0 to 3 K from the boundary layer to 5 km in deep convective updraft cores for four CRM simulations and all LAM simulations, whereas the environmental MSE decreases by 10 to 13 K. The 90th percentile of maximum MSE even increases by 1 to 2.5 K just above the freezing level as a result of substantial latent heat release by freezing liquid water.

With minimal entrainment, simulated deep updraft cores have buoyancy reduction by water loading that is equal to or greater than that by entrainment in contrast to some studies that suggest observed tropical oceanic updrafts penetrate through midlevels by unloading condensate in the face of appreciable entrainment [*Wei et al.*, 1998; *Zipser*, 2003]. *Bryan et al.* [2003] and *Craig and Dörnbrack* [2008] conclude that a 1-km horizontal mesh in simulations is insufficient to resolve buoyancy in convective clouds, while several other studies [*Petch and Gray*, 2001; *Adlerman and Droegemeier*, 2002; *Petch et al.*, 2002; *Khairoutdinov et al.*, 2009; *Dawson et al.*, 2010; *Bryan and Morrison*, 2012] also note sensitivities of convective properties to horizontal grid spacing less than 1 km. To test the effects of grid spacing, two quarter domain (88 km by 88 km size) DHARMA-2 M simulations were performed, one using ~100 m horizontal grid spacing and ~100 m or better vertical grid spacing throughout the troposphere, and the other using the original ~900 m horizontal grid spacing and double the vertical grid spacing. Results from these new simulations show that increased resolution produces greater entrainment at low and middle levels, which delays the transition from shallow to deep convection as found in *Khairoutdinov and Randall* [2006]. This increased entrainment does not greatly lessen full resolution maximum MSE values at midlevels, although values are somewhat decreased when the 100 m simulation is degraded to 900 m, as shown in Figures 17a and 17b. The larger effect is that deep convective cores in which $w > 10$ m s^{-1} change from resembling a plume in ~1-km simulations (Figure 17c) to resembling bubble-like cores of shedding thermals in the ~100 m simulation (Figures 17a and 17b), which decreases the spatial dimensions of cores and make them more numerous. As shown in Figures 17d–17f, the spatial heterogeneity of condensate is also increased, which likely increases the probability of sedimentation out of updraft cores.

Figure 18 shows cumulative distributions of the contribution of 10-km altitude *w* values to upward mass flux, condensate contents to total condensate, and upward condensate fluxes to total upward condensate flux for the 1310*Z*–1750*Z* dual-Doppler retrieval period. The ~900 m simulation has 24% more condensate, 15% greater upward mass flux, and 29% greater upward flux of condensate than the ~100 m simulation degraded

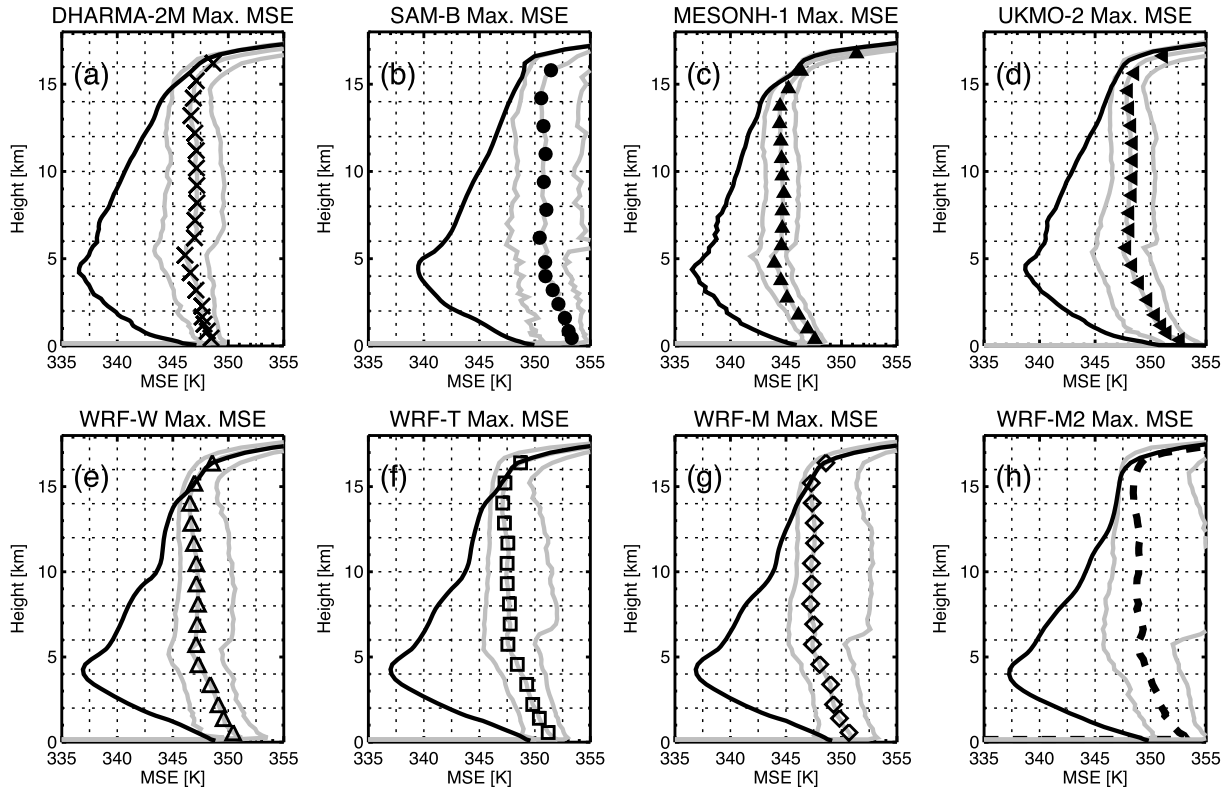

Figure 16. Shown are profiles of moist static energy for four CRM simulations: (a) DHARMA-2 M, (b) SAM-B, (c) MESONH-1, and (d) UKMO-2, and four LAM simulations: (e) WRF-W, (f) WRF-T, (g) WRF-M, and (h) WRF-M2. The domain mean (environmental) profiles are shown in black, while the median profiles of maximum moist static energy in deep convective updrafts as in Figure 9 are shown with gray lines and symbols. The 10th and 90th percentiles from the simulations are shown with gray lines.

to ~900 m grid spacing. Figure 18 shows that these differences are almost entirely a result of differences in simulated w values greater than 10 m s^{-1} or condensates greater than 3 g m^{-3}. For periods of less intense convection later in the event, the two simulations have negligible differences. Thus, increasing resolution results in a weakening of the most intense convection but not enough of a weakening to match radar retrievals of w and reflectivity (not shown). These results are likely sensitive to the model setup and the event being simulated. Therefore, more comparisons of CRMs and LAMs to large eddy simulations (LES) and observations should be performed in future studies.

Another production mechanism for overly strong updrafts is inaccurate representation of the large-scale environment leading to incorrect convective morphology. As previously discussed in section 4.1, simulations fairly accurately represent mean thermodynamic and wind vertical profiles. Observed and simulated vertical wind shear and instability values, however, are sufficient for midlatitude continental supercellular convection [*Thompson et al*., 2003]. Therefore, it may not be surprising that some of the strongest simulated updrafts can be described as supercellular, as they are deeply rotating, long lived, and produce midlevel pressure perturbations of 1–2 hPa that cause the cells to deviate to the left of the mean movement of the more common cells [*Rotunno and Klemp*, 1984]. One such cell from the DHARMA-2 M simulation is circled in Figure 19a, and a zonal vertical cross section through it at an earlier time is shown in Figure 20. This is not a symptom of model setup because cells with these characteristics are also present in the LAM simulations, as shown by the cell in the WRF-M2 simulation circled in Figure 19b. In these strong left moving updrafts, Figure 20 shows that a strong vertical pressure gradient force is produced by a shear-induced 1–2 hPa midlevel negative pressure perturbation, which accelerates the updraft to 10–15 m s^{-1} despite negative or neutral buoyancy resulting from large water loading shown in Figures 20a–20c. Low- and middle-level entrainment is very limited in the upshear portion of the updraft (see Figure 15a) because it is protected by midlevel positive pressure perturbations in Figure 20d caused by the interaction of the easterly flow with the slower moving updraft [*Barnes*, 1969; *Wilhelmson*, 1974; *Ramond*, 1978; *Heymsfield et al*., 1978]. As can be seen

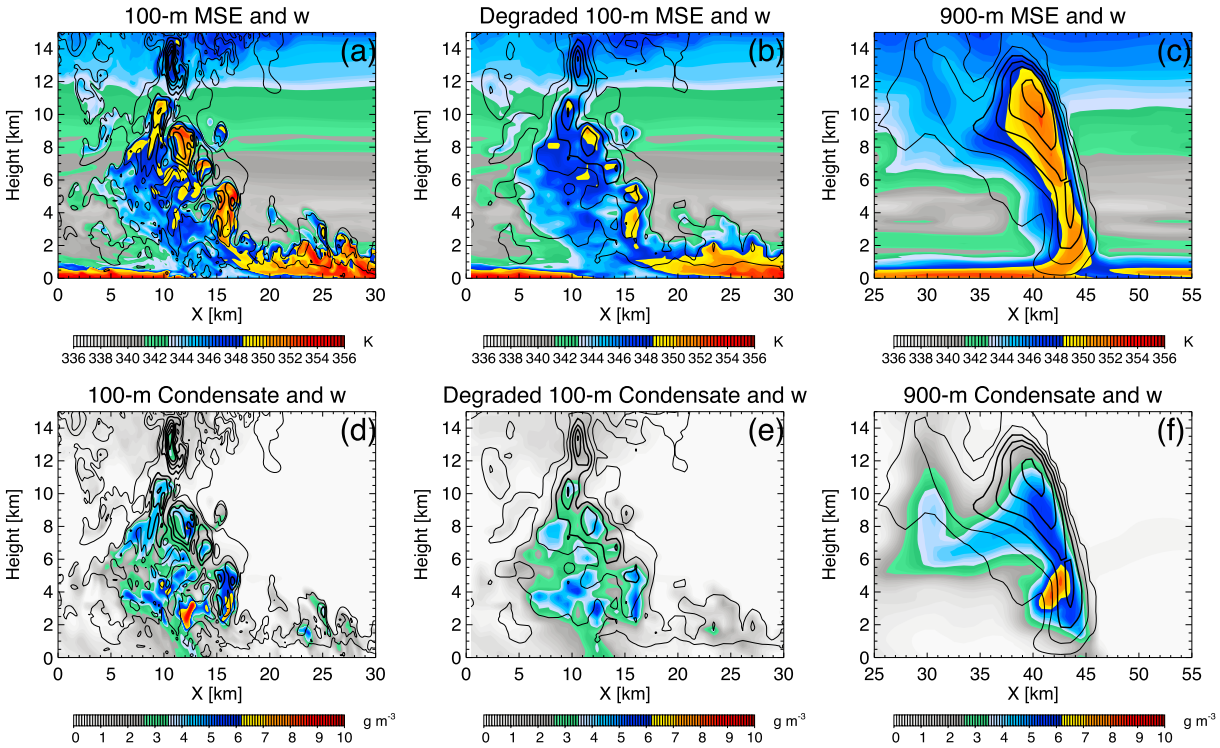

Figure 17. Example vertical cross sections through deep updrafts in quarter domain DHARMA-2 M simulations showing (a–c) MSE (filled) and (d–f) total condensate (filled) with vertical velocity (thin black contours: 1 and 5 m s^{-1}; thick black contours: 10, 15, 20, and 25 m s^{-1}) overplotted. The 100 m run is shown in Figures 17a and 17d, the 100 m run degraded to 900 m in Figures 17b and 17e, and the 900 m run in Figures 17c and 17f. Note that the MSE scale is slightly changed from Figure 14 because the 100 m run cross sections are shown for an earlier time when boundary layer MSE was greater.

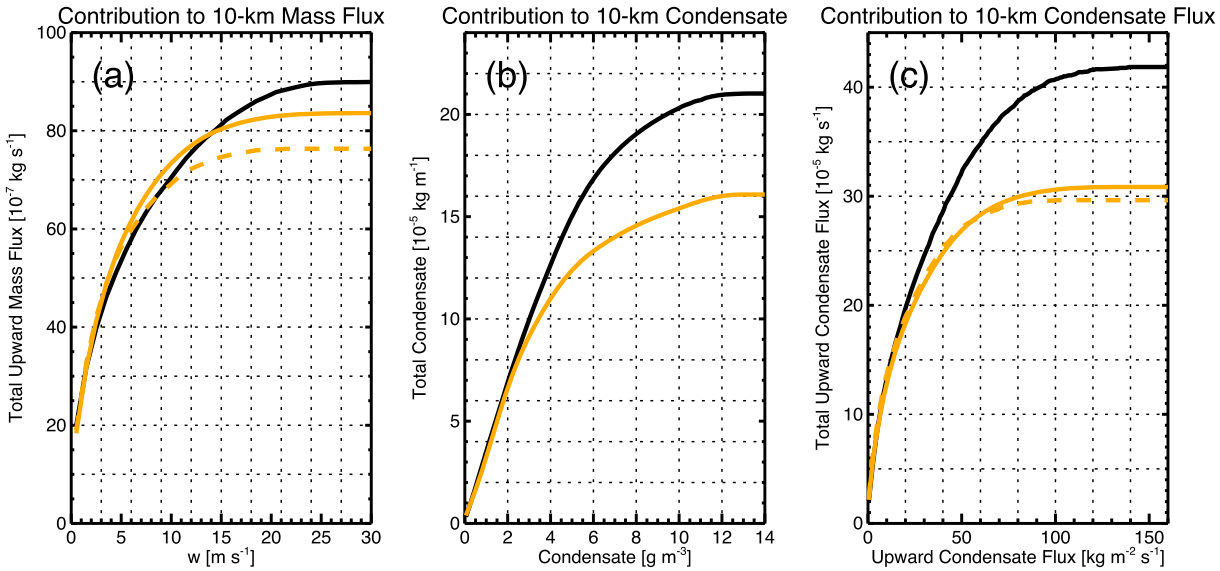

Figure 18. Cumulative distributions of the contribution of 10 km altitude (a) vertical velocity values to total upward mass flux, (b) condensate contents to total condensate, and (c) upward condensate fluxes to total upward condensate flux for the 1310*Z* to 1750*Z* period on 23 January 2006 in DHARMA-2 M quarter domain (88 km by 88 km) simulations. The ~900 m horizontal grid spacing, 96 vertical level simulation is shown in black, the ~100 m horizontal grid spacing, 192 vertical level high-resolution simulation in solid orange, and the high-resolution simulation degraded to a horizontal grid spacing of ~900 m in dashed orange.

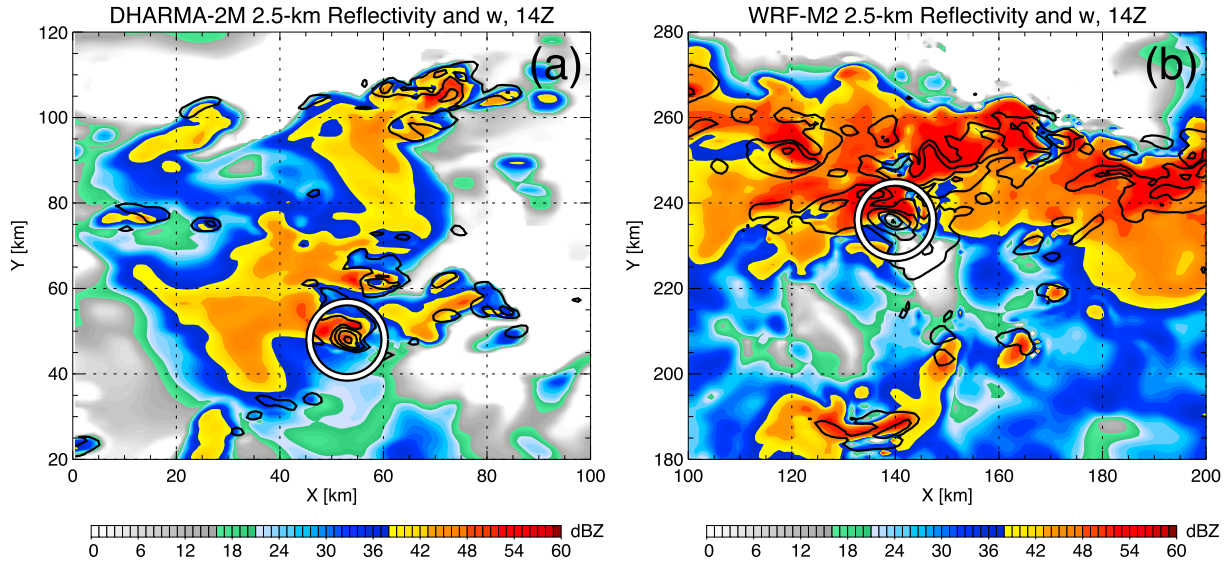

Figure 19. The 2.5 km altitude horizontal cross sections at 14*Z* 23 January 2006 for (a) DHARMA-2 M and (b) WRF-M2 showing radar reflectivity (filled) and vertical velocity (black contours: 1, 5, 10, 15, and 20 m s^{-1}) with supercellular cells circled. The full CRM domain is ~3 times larger, and the inner LAM domain ~15 times larger than the 100 km by 100 km cross sections shown.

in the water-loading acceleration field shown in Figure 20b, the peak amounts of condensate are located slightly downshear (to the left) of the peak vertical velocities with some of it exiting the updraft, mixing with environmental air and fueling a weak convective downdraft that increases the horizontal gradient in *w* and tilting and stretching of environmental horizontal vorticity. Despite sedimentation of some rain out of the updraft, the core remains strong enough to loft substantial RWC above the −4°C level, where most of it freezes over less than a 1-km depth, releasing a significant amount of latent heat that contributes to excessive upper tropospheric peak *w*.

This is shown in Figure 21 with results from two WRF-M2 sensitivity simulations that were performed to test the impact of freezing condensate on upper tropospheric *w*: one in which freezing of rainwater is not allowed to increase temperature and a second in which the freezing of both rainwater and cloud water are not allowed to increase temperature. All else in these simulations is held the same as the baseline WRF-M2 simulation. Statistics in Figure 21 based on ~1400 simulated deep updrafts show that the 90th percentile of maximum buoyancy in WRF-M2 deep updrafts (solid gray) increases from less than 0.1 m s^{-2} at 6 km to 0.11 m s^{-2} at 6.5 km. Both sensitivity simulations (dotted blue and dashed orange) eliminate this maximum buoyancy increase. The 90th percentile of maximum thermal buoyancy alone (not shown) increases from less than 0.15 m s^{-2} to 0.18 m s^{-2} over a ~500 m depth due to the freezing of rain. The strong deep updrafts in WRF-M2 maintain greater buoyancy than in the two sensitivity simulations throughout the upper troposphere because of temperature increases associated with freezing of rainwater. Although not shown, these differences are smaller in the 50th percentile and greater in the 99th percentile of maximum buoyancy because stronger updrafts have more rain that is lofted and frozen. Removal of the latent heat of fusion for freezing rainwater in strong updraft cores decreases the peak in the 90th percentile of maximum *w* by 10 m s^{-1} and the 90th percentile of maximum radar reflectivity by 5 dBZ throughout the upper troposphere in Figure 21. The largest effect of freezing cloud water is above 10 km where the 90th percentile maximum buoyancy and *w* are greater in the simulation that removes the latent heat of fusion for only rainwater rather than all liquid water (dotted blue). The effect of cloud water is smaller than that of rain because much more rain is lofted and frozen in the core of the updraft, which leads to peak freezing rates that are an order of magnitude higher for rain than cloud water (not shown). Although removing the latent heat of freezing is unphysical, doing so shows that it is a primary cause for simulated extreme upper tropospheric vertical velocities.

Instability and vertical shear decrease between 15 and 18*Z*, which decreases the number of cells with supercellular characteristics and allows cold pools to exert a larger control on convective evolution with cells moving more northward in broken lines (not shown). An in-depth analysis of cold pool properties was not

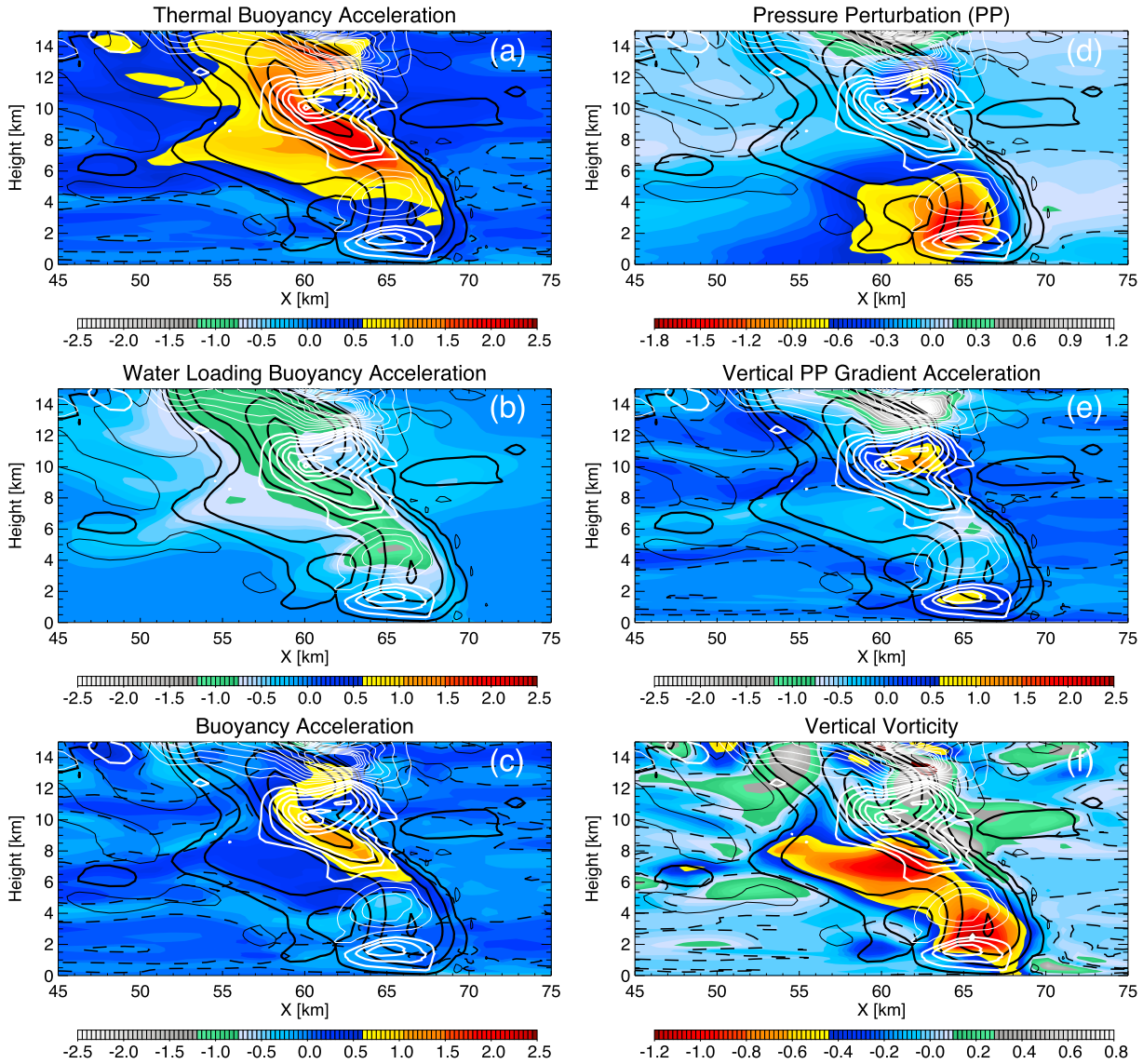

Figure 20. Example vertical cross sections through a strong long-lived left moving deep convective updraft in the DHARMA-2 M simulation (the one circled in Figure 19a) at 1320*Z* showing (a) thermal buoyancy acceleration [1×10^{-1} m s^{-2}], (b) water-loading buoyancy acceleration [1×10^{-1} m s^{-2}], (c) total buoyancy acceleration [1×10^{-1} m s^{-2}], (d) pressure perturbation [hPa], (e) vertical pressure perturbation gradient acceleration [1×10^{-1} m s^{-2}], and (f) vertical vorticity [1×10^{-2} s^{-1}]. Zero lines are shown in dashed black, vertical velocity (−5, −1, 1, 5, 10, 15, 20, 25, and 30 m s^{-1}) is contoured in solid black (upward is thick and downward thin), and *Dw*/*Dt* (every 0.02 m s^{-2}) is contoured in white. Cell motion and 0–6 km shear are primarily from right to left (westward).

performed because observations sufficient for comparison to simulations are not available, but future field campaigns should focus on obtaining cold pool observations for model validation. Despite being generally weaker than left moving cells because of weaker midlevel negative pressure perturbations (not shown), more numerous right moving cells are able to maintain vertically coherent cores of nearly constant MSE and have significant amounts of condensate (greater than 4 g m^{-3}) above the freezing level, as shown in Figure 22. Midlevel vertical velocities of 10 m s^{-1} greater than rain mass fall speeds of 4–8 m s^{-1} allow lofting and freezing of a significant amount of rain, which fuels strong upper tropospheric vertical velocities greater than 30 m s^{-1}, only slightly less than the peak *w* (40 m s^{-1}) of the updraft in Figure 20 (not shown). Total condensate values in the Figure 20 updraft are also larger than the updraft in Figure 22 with greater than 5 g m^{-3} above the freezing level and 9 g m^{-3} just below it (not shown), whereas the updraft in Figure 22 has a peak total condensate of 6 g m^{-3}. These differences are likely related to additional low-level lift produced by midlevel pressure perturbations in the left moving cell, which allows that updraft to reach 15 m s^{-1} by the

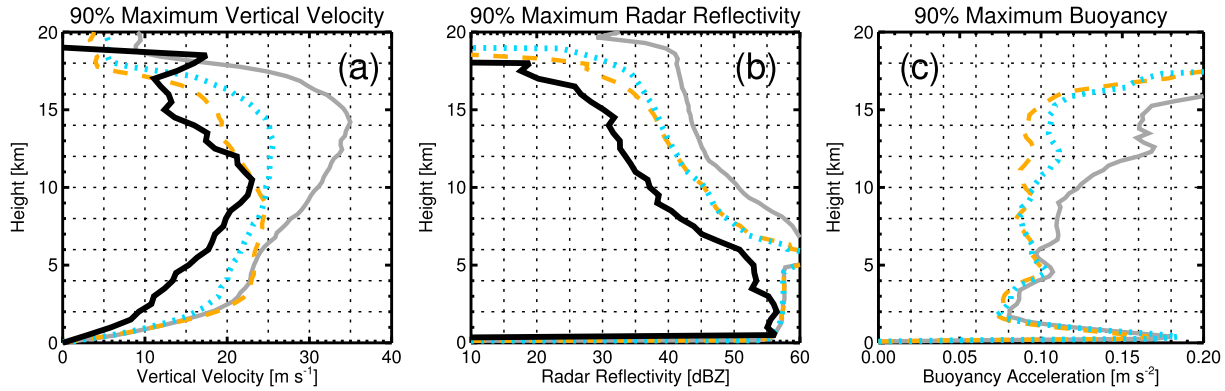

Figure 21. The 90th percentile of (a) maximum vertical velocity, (b) maximum radar reflectivity, and (c) maximum buoyancy in deep convective updrafts as in Figure 8 for WRF-M2 and dual-Doppler retrievals. WRF-M2 is shown in solid gray, WRF-M2 without the latent heat of fusion for rain in dotted blue, WRF-M2 without the latent heat of fusion for liquid water (rain and cloud water) in dashed orange, and observations in solid black. Simulated updraft samples are taken from the entire inner domain over the entire event lifetime to accumulate a large sample of ~1400 updrafts. Sixty observed updraft samples are taken within the dual-Doppler lobes between 1310*Z* and 1750*Z* on 23 January 2006 with their 90th percentile reflectivity and vertical velocity shown for context.

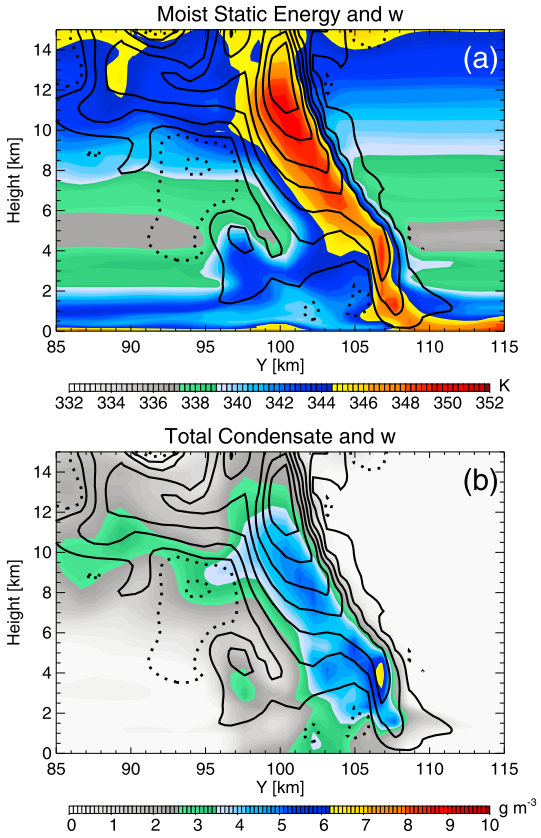

Figure 22. Example vertical cross sections through a strong right moving deep convective updraft in the DHARMA-2 M simulation (the one at $x = 70$ km and $y = 110$ km in Figure 19a) at 1350*Z* showing (a) moist static energy [K], and (b) total condensate [g m^{-3}] color filled with vertical velocity (-5, -1, 1, 5, 10, 15, 20, 25, and 30 m s^{-1}) contoured in solid black (upward is thick and downward is thin). Cell motion is primarily from left to right and into the cross sections (northwestward). The 0–6 km shear is primarily into the cross section (westward).

time it reaches 3-km altitude, whereas the right moving updraft has only reached 10 m s^{-1} at this point. Furthermore, the 10 m s^{-1} or greater portion of the left moving updraft is ~4 km wide at low to middle levels, whereas it is half this wide in the right moving updraft.

5. Conclusions

Atmospheric models always confront limits of spatiotemporal resolution and necessarily simplified representation of hydrometeor properties and process rates. Such models may be far from maximizing their predictive abilities at a given resolution, however. At cloud-resolving scales, improvements are possible in advection techniques, turbulent mixing schemes, land surface schemes, and a focus of this study, microphysics schemes. In the case of microphysics, there are new ice multiplication processes still being hypothesized and many microphysics processes in models remain poorly constrained due to a lack of observations [*Stephens*, 2005] among other deficits. Additionally, there is a scarcity of robust comparisons between simulated and observed convective vertical wind speeds, even though these wind speeds are crucial to vertical transport of aerosol and water vapor and help determine microphysical properties within a convective updraft and detrained anvil. Output from high-resolution simulations is used in satellite retrievals and for improving representation of convective systems in GCMs. It is therefore prudent to obtain more high-quality convective observations and perform more rigorous comparisons of them with simulation output.

Detailed comparison of CRM and LAM simulations of the 23–24 January 2006 active monsoonal MCS during TWP-ICE with vertical wind retrievals of the same event during the multicellular convective buildup stage of the event (1310–1750*Z* 23 January) show the cause for high biased radar reflectivity aloft reported in *Varble et al.* [2011] is likely attributable to more than poorly parameterized ice microphysics. Microphysics assumptions modulate this high bias by altering the distribution of condensate mass between different hydrometeor species and the sizes of hydrometeors, but simulated deep convective updrafts that are too strong and produce too much lofted condensate appear central to the presence of the bias in all 14 simulations. Without significant sample sizes of in situ observed convective properties, it is difficult to definitively establish that simulated convective updrafts are stronger than observed, but ample evidence has been shown here to support this conclusion, including comparisons with 3-D radar reflectivity and vertical velocity from a dual-Doppler retrieval and comparison of convective vertical velocity and condensate statistics with previous studies. Overly intense simulated updrafts are weakened in a 100 m horizontal and vertical grid spaced quarter domain DHARMA-2 M simulation, but not enough to match observational retrievals. The overly strong convection appears to be additionally linked to some mixture of insufficient grid spacing, model forcing biases, and interactions between dynamics and microphysics that promote stronger convection than occurred in reality. This conclusion is true for both CRM and LAM simulations, which use different domain sizes, boundary conditions, and large-scale forcings, but produce very similar convective and stratiform biases. Models need to predict convective strength through the MCS life cycle accurately because it impacts cloud and precipitation properties including the partitioning of convective, stratiform, and anvil regions.

Problems are apparent in the warm region of simulated deep convective updrafts where not enough rain is falling out of large cores with high vertical wind speeds. Some of the most intense updrafts are nearly undilute and exhibit supercellular characteristics, even though domain mean thermodynamic and wind profiles are similar in simulations and observations. Large RWCs in simulated deep updraft cores are lofted above the −4°C level and frozen, which increases maximum vertical velocity throughout the upper troposphere, contributing to simulated convective area and radar reflectivity aloft that is biased high. These biases were found in previous studies and primarily attributed to incorrect ice size and categorization of hydrometeors, but evidence presented here shows that errors in convective dynamics and total water content can also contribute to the high bias. In addition to graupel, constant density, spherical *m-D* snow in two-moment form contributes to the high bias in reflectivity, but an *m-D* relationship that is more realistic with mass proportional to $\sim D^2$ can reduce the bias. Using hail rather than graupel reduces the amount of precipitating dense ice at upper levels because hail falls out more quickly than graupel, but it also significantly increases the amount of snow at upper levels. Regardless of the dense ice species chosen, very large liquid water contents are lofted and frozen in updraft cores within all simulations, which lead to peak vertical wind speeds in the upper troposphere that are far in excess of those retrieved by radars. These high-condensate contents and vertical wind speeds need to be further studied in the context of large-scale environment, model forcing, grid spacing, and subgrid-scale parameterization sensitivities. As computing power increases, LES setups with bin microphysics in mesoscale simulations will become useful in validating coarser, more parameterized simulations, but these setups will also need observational constraint and accurate characterization of the large-scale environment to be fully utilized.

This study is not without caveats, the largest being the use of CRMs with periodic lateral boundaries and domains too small to fully capture the size of a large MCS such as the one on 23–24 January 2006 during TWP-ICE. The CRM domain size is limited by the derived large-scale advective tendencies that become less accurate with increasing sounding array size and less radar coverage, but as is discussed more in Part 2, the limited domain size negatively impacts stratiform rainfall. However, as shown in *Varble et al.* [2011], smaller mesoscale precipitation events earlier in the active monsoon period of TWP-ICE also exhibit biases, and convective biases show up well before the event becomes organized. Additionally, the LAM simulations with nested larger domains have the ability to represent this large MCS event, yet exhibit many of the same biases as the CRMs. LAMs, however, have their own biases imposed by inaccuracies in the large-scale analysis chosen to force them, which is discussed more in Part 2. Results in this study are also sensitive to the definitions of convective and stratiform regions, deep updrafts, and the accuracy of observations. More observations are needed within tropical convective updrafts, specifically aircraft in situ and vertical profiling vertical velocity and microphysics observations between low levels and the mixed phase region within a region well characterized by scanning precipitation radar(s) and soundings to test and improve radar retrievals and high-resolution models.

Acknowledgments

This research was supported by the Department of Energy's Atmospheric System Research program, award DEFG0208ER64557, Program Manager Ashley Williamson, with computing resources provided by the Center for High Performance Computing at the University of Utah. Simulations are available for download in the ARM archive (www.archive.arm.gov) or from Adam Varble (a.varble@utah.edu), and the dual-Doppler retrieval is available from Scott Collis (scollis@anl.gov). Special thanks are given to Peter May at the Centre for Australian Weather and Climate Research and the Australian Bureau of Meteorology for providing the CPOL radar data and derived rain rates. DHARMA simulations were supported by the DOE Office of Science, Office of Biological and Environmental Research, through Interagency agreement DE-AI02-06ER64173 and contract DE-FG03-02ER63337, the NASA Radiation Sciences Program, the DOE National Energy Research Scientific Computing Center, and the NASA Advanced Supercomputing Division. Ping Zhu wishes to acknowledge his support from the DOE ASR program under grant DE-FG02-09ER64737. Jiwen Fan also thanks the support from the DOE ASR program. PNNL is operated for DOE by Battelle Memorial Institute under contract DE-AC05-76RL01830. The contribution of Scott Collis through Argonne National Laboratory was supported by the U.S. Department of Energy, Office of Science, Office of Biological and Environmental Research, under contract DE-AC02-06CH11357 and was funded through the ARM program. We would also like to thank three anonymous reviewers for comments that improved the quality of the manuscript.

References

Ackerman, A., O. Toon, D. Stevens, A. Heymsfield, V. Ramanathan, and E. Welton (2000), Reduction of tropical cloudiness by soot, *Science*, *288*(5468), 1042–1047, doi:10.1126/science.288.5468.1042.

Adlerman, E. J., and K. K. Droegemeier (2002), The sensitivity of numerically simulated cyclic mesocyclogenesis to variations in model physical and computational parameters, *Mon. Weather Rev.*, *130*(11), 2671–2691.

Barnes, S. L. (1969), Some aspects of a severe, right-moving thunderstorm, deduced from mesonetwork rawinsonde observations, *J. Atmos. Sci.*, *27*, 634–648.

Bechtold, P., et al. (2000), A GCSS model intercomparison for a tropical squall line observed during TOGA-COARE. II: Intercomparison of single-column models and a cloud-resolving model, *Q. J. R. Meteorol. Soc.*, *126*(564), 865–888, doi:10.1002/qj.49712656405.

Blossey, P. N., C. S. Bretherton, J. Cetrone, and M. Kharoutdinov (2007), Cloud-resolving model simulations of KWAJEX: Model sensitivities and comparisons with satellite radar observations, *J. Atmos. Sci.*, *64*(5), 1488–1508, doi:10.1175/JAS3982.1.

Bryan, G. H., and H. Morrison (2012), Sensitivity of a simulated squall line to horizontal resolution and parameterization of microphysics, *Mon. Weather Rev.*, *140*(1), 202–225.

Bryan, G. H., J. C. Wyngaard, and J. M. Fritsch (2003), Resolution requirements for the simulation of deep moist convection, *Mon. Weather Rev.*, *131*, 2394–2416.

Bryan, G. H., J. C. Knievel, and M. D. Parker (2006), A multimodel assessment of RKW Theory's relevance to squall-line characteristics, *Mon. Weather Rev.*, *134*, 2772–2792.

Caine, S., T. P. Lane, P. T. May, C. Jakob, S. T. Siems, M. J. Manton, and J. Pinto (2013), Statistical assessment of tropical convection-permitting model simulations using a cell-tracking algorithm, *Mon. Weather Rev.*, *141*(2), 557–581.

Cifelli, R., and S. A. Rutledge (1998), Vertical motion, diabatic heating, and rainfall characteristics in north Australian convective systems, *Q. J. R. Meteorol. Soc.*, *124*, 1133–1162.

Collis, S., A. Protat, P. T. May, and C. Williams (2013), Statistics of storm updraft velocities from TWP-ICE including verification with profiling measurements, *J. Appl. Meteorol. Climatol.*, *52*, 1909–1922.

Cox, G. P. (1988), Modelling precipitation in frontal rainbands, *Q. J. R. Meteorol. Soc.*, *114*, 115–127.

Craig, G. C., and A. Dörnbrack (2008), Entrainment in cumulus clouds: What resolution is cloud-resolving?, *J. Atmos. Sci.*, *65*, 3978–3988.

Davies, L., et al. (2013), A single-column model ensemble approach applied to the TWP-ICE experiment, *J. Geophys. Res. Atmos.*, *118*, 6544–6563, doi:10.1002/jgrd.50450.

Dawson, D. T., M. Xue, J. A. Milbrandt, and M. K. Yau (2010), Comparison of evaporation and cold pool development between single-moment and multimoment bulk microphysics schemes in idealized simulations of tornadic thunderstorms, *Mon. Weather Rev.*, *138*(4), 1152–1171.

Del Genio, A. D., and W. Kovari (2002), Climatic properties of tropical precipitating convection under varying environmental conditions, *J. Clim.*, *15*, 2597–2615.

Del Genio, A. D., J. Wu, and Y. Chen (2012), Characteristics of mesoscale organization in WRF simulations of convection during TWP-ICE, *J. Clim.*, *25*, 5666–5688, doi:10.1175/JCLI-D-11-00422.1.

Dudhia, J. (1989), Numerical study of convection observed during the Winter Monsoon Experiment using a mesoscale two-dimensional model, *J. Atmos. Sci.*, *46*, 3077–3107.

Field, P. R., R. J. Hogan, P. R. A. Brown, A. J. Illingsworth, T. W. Choularton, and R. J. Cotton (2005), Parameterization of ice-particle size distributions for mid-latitude stratiform cloud, *Q. J. R. Meteorol. Soc.*, *131*, 1997–2017.

Fowler, L. D., D. A. Randall, and S. A. Rutledge (1996), Liquid and ice cloud microphysics in the CSU general circulation model. Part I: Model description and simulated microphysical processes, *J. Clim.*, *9*, 489–529.

Fridlind, A., A. Ackerman, J. Petch, P. Field, A. Hill, G. McFarquhar, S. Xie, and M. Zhang (2010), ARM/GCSS/SPARC TWP-ICE CRM intercomparison study, *NASA/TM-2010-215858*, NASA, Greenbelt, Md.

Fridlind, A. M., et al. (2012), A comparison of TWP-ICE observational data with cloud-resolving model results, *J. Geophys. Res.*, *117*, D05204, doi:10.1029/2011JD016595.

Ghan, S. J., L. R. Leung, and Q. Hu (1997), Application of cloud microphysics to NCAR community climate model, *J. Geophys. Res.*, *102*, 16,507–16,527, doi:10.1029/97JD00703.

Ghan, S. J., et al. (2000), An intercomparison of single column model simulations of summertime midlatitude continental convection, *J. Geophys. Res.*, *105*, 2091–2124, doi:10.1029/1999JD90071.

Gilmore, M. S., J. M. Straka, and E. N. Rasmussen (2004), Precipitation uncertainty due to variations in precipitation particles parameters within a simple microphysics scheme, *Mon. Weather Rev.*, *132*, 2610–2627.

Grabowski, W. W. (1999), A parameterization of cloud microphysics for long-term cloud-resolving modeling of tropical convection, *Atmos. Res.*, *52*(1–2), 17–41, doi:10.1016/S0169-8095(99)00029-0.

Grabowski, W. W. (2001), Coupling cloud processes with the large-scale dynamics using the cloud-resolving convection parameterization (CRCP), *J. Atmos. Sci.*, *58*, 978–997.

Grabowski, W. W., et al. (2006), Daytime convective development over land: A model intercomparison based on LBA observations, *Q. J. R. Meteorol. Soc.*, *132*(615), 317–344, doi:10.1256/qj.04.147.

Gray, M. E. B., J. Petch, S. H. Derbyshire, A. R. Brown, A. P. Lock, H. A. Swann, and P. R. A. Brown (2001), Version 2.3 of the Met Office large eddy model: Part II. Scientific documentation, Met O (APR) Turbulence and Diffusion Note No. 276.

Hartmann, D. L., H. H. Hendon, and R. A. Houze Jr. (1984), Some implications of the mesoscale circulations in tropical cloud clusters for large-scale dynamics and climate, *J. Atmos. Sci.*, *41*, 113–121.

Heymsfield, A. J., P. N. Johnson, and J. E. Dye (1978), Observations of moist adiabatic ascent in northeast Colorado cumulus congestus clouds, *J. Atmos. Sci.*, *35*, 1689–1703.

Heymsfield, A. J., A. Bansemer, G. Heymsfield, and A. O. Fierro (2009), Microphysics of maritime tropical convective updrafts at temperatures from −20° to −60°, *J. Atmos. Sci.*, *66*, 3530–3562, doi:10.1175/2009JAS3107.1.

Heymsfield, G. M., L. Tian, A. J. Heymsfield, L. Li, and S. Guimond (2010), Characteristics of deep tropical and subtropical convection from nadir-viewing high-altitude airborne Doppler radar, *J. Atmos. Sci.*, *67*, 285–308, doi:10.1175/2009JAS3132.1.

Hong, S.-Y., and J.-O. J. Lim (2006), The WRF single-moment 6-class microphysics scheme (WSM6), *J. Korean Meteorol. Soc.*, *42*, 129–151.

Hong, S.-Y., Y. Noh, and J. Dudhia (2006), A new vertical diffusion package with an explicit treatment of entrainment processes, *Mon. Weather Rev.*, *134*, 2318–2341.

Houze, R. A., Jr. (1982), Cloud clusters and large-scale vertical motions in the tropics, *J. Meteorol. Soc. Jpn.*, *60*(1), 396–410.

Houze, R. A., Jr. (1989), Observed structure of mesoscale convective systems and implications for large-scale heating, *Q. J. R. Meteorol. Soc.*, *115*(487), 425–461, doi:10.1002/qj.49711548702.

Houze, R. A., Jr. (1997), Stratiform precipitation in regions of convection: A meteorological paradox?, *Bull. Am. Meteorol. Soc.*, *78*(10), 2179–2196.
Houze, R. A., Jr. (2004), Mesoscale convective systems, *Rev. Geophys.*, *42*, RG4003, doi:10.1029/2004RG000150.
Houze, R. A., Jr., P. V. Hobbs, P. H. Herzegh, and D. B. Parsons (1979), Size distributions of precipitation particles in frontal clouds, *J. Atmos. Sci.*, *36*, 156–162.
Houze, R. A., Jr., W.-C. Lee, and M. M. Bell (2009), Convective contribution to the genesis of Hurricane Ophelia, *Mon. Weather Rev.*, *137*, 2778–2800.
Johnson, R. H. (1984), Partitioning tropical heat and moisture budgets into cumulus and mesoscale components: Implications for cumulus parameterization, *Mon. Weather Rev.*, *112*(8), 1590–1601.
Jorgensen, D. P., and M. A. LeMone (1989), Vertical velocity characteristics of oceanic convection, *J. Atmos. Sci.*, *46*(5), 621–640.
Kain, J. S. (2004), The Kain-Fritsch convective parameterization: An update, *J. Appl. Meteorol.*, *43*, 170–181.
Keenan, T. D., and R. E. Carbone (1992), A preliminary morphology of precipitation systems in tropical northern Australia, *Q. J. R. Meteorol. Soc.*, *118*(504), 283–326, doi:10.1002/qj.49711850406.
Keenan, T. D., K. Glasson, F. Cummings, T. S. Bird, J. Keeler, and J. Lutz (1998), The BMRC/NCAR C-band polarimetric (C-POL) radar system, *J. Atmos. Oceanic Technol.*, *15*(4), 871–886.
Khairoutdinov, M., and D. Randall (2003), Cloud resolving modeling of the ARM summer 1997 IOP: Model formulation, results, uncertainties, and sensitivities, *J. Atmos. Sci.*, *60*(4), 607–625.
Khairoutdinov, M. F., and D. A. Randall (2001), A cloud resolving model as a parameterization in the NCAR Community Climate System Model: Preliminary results, *Geophys. Res. Lett.*, *28*, 3617–3620, doi:10.1029/2001GL013552.
Khairoutdinov, M. F., and D. A. Randall (2006), High-resolution simulation of shallow-to-deep convection transition over land, *J. Atmos. Sci.*, *63*, 3421–3436.
Khairoutdinov, M. F., S. K. Krueger, C.-H. Moeng, P. A. Bogenschutz, and D. A. Randall (2009), Large-eddy simulation of maritime deep tropical convection, *J. Adv. Model. Earth Syst.*, *1*, 15, doi:10.3894/JAMES.2009.1.15.
Kingsmill, D. E., S. E. Yuter, A. J. Heymsfield, P. V. Hobbs, A. V. Korolev, J. L. Stith, A. Bansemer, J. A. Haggerty, and A. L. Rangno (2004), TRMM common microphysics products: A tool for evaluating spaceborne precipitation retrieval algorithms, *J. Appl. Meteorol.*, *43*, 1598–1618.
Kummerow, C., Y. Hong, W. S. Olson, S. Yang, R. F. Adler, J. McCollum, R. Ferraro, G. Petty, D.-B. Shin, and T. T. Wilheit (2001), The evolution of the Goddard Profiling Algorithm (GPROF) for rainfall estimation from passive microwave sensors, *J. Appl. Meteorol.*, *40*, 1801–1820.
Lafore, J. P., et al. (1998), The Meso-NH atmospheric simulation system. Part I: Adiabatic formulation and control simulations, *Ann. Geophys.*, *16*, 90–109, doi:10.1007/s00585-997-0090-6.
Lang, S., W.-K. Tao, J. Simpson, and B. Ferrier (2003), Modeling of convective–stratiform precipitation processes: Sensitivity to partitioning methods, *J. Appl. Meteorol.*, *42*, 505–527, doi:10.1175/1520-0450(2003)042<0505:MOCSPP>2.0.CO;2.
Lang, S., W.-K. Tao, J. Simpson, R. Cifelli, S. Rutledge, W. Olson, and J. Halverson (2007), Improving simulations of convective systems from TRMM LBA: Easterly and westerly regimes, *J. Atmos. Sci.*, *64*(4), 1141–1164, doi:10.1175/JAS3879.1.
Lang, S. E., W.-K. Tao, X. Zeng, and Y. Li (2011), Reducing the biases in simulated radar reflectivities from a bulk microphysics scheme: Tropical convective systems, *J. Atmos. Sci.*, *68*, 2306–2320.
Lawson, R. P., E. Jensen, D. L. Mitchell, B. Baker, Q. Mo, and B. Pilson (2010), Microphysical and radiative properties of tropical clouds investigated in TC4 and NAMMA, *J. Geophys. Res.*, *115*, D00J08, doi:10.1029/2009JD013017.
Li, Y., E. J. Zipser, S. K. Krueger, and M. A. Zulauf (2008), Cloud-resolving modeling of deep convection during KWAJEX: Part I: Comparison to TRMM satellite and ground-based observations, *Mon. Weather Rev.*, *136*, 2699–2712, doi:10.1175/2007MWR2258.1.
Locatelli, J. D., and P. V. Hobbs (1974), Fall speeds and masses of solid precipitation particles, *J. Geophys. Res.*, *79*, 2185–2197, doi:10.1029/JC079i015p02185.
Lohmann, U., and E. Roeckner (1996), Design and performance of a new cloud microphysics scheme developed for the ECHAM general circulation model, *Clim. Dyn.*, *12*, 557–572.
Luo, Y., Y. Wang, H. Wang, Y. Zheng, and H. Morrison (2010), Modeling convective-stratiform precipitation processes on a Mei-Yu front with the Weather Research and Forecasting model: Comparison with observations and sensitivity to cloud microphysics parameterizations, *J. Geophys. Res.*, *115*, D18117, doi:10.1029/2010JD013873.
Mapes, B. E., and R. A. Houze Jr. (1995), Diabatic divergence profiles in western Pacific mesoscale convective systems, *J. Atmos. Sci.*, *52*, 1807–1828.
Matsui, T., X. Zeng, W.-K. Tao, H. Masunaga, W. S. Olson, and S. Lang (2009), Evaluation of long-term cloud-resolving model simulations using satellite radiance observations and multifrequency satellite simulators, *J. Atmos. Oceanic Technol.*, *26*(7), 1261–1274, doi:10.1175/2008JTECHA1168.1.
May, P. T., and A. Ballinger (2007), The statistical characteristics of convective cells in a monsoon regime (Darwin, Northern Australia), *Mon. Weather Rev.*, *135*, 82–92, doi:10.1175/MWR3273.1.
May, P. T., and D. K. Rajopadhyaya (1999), Vertical velocity characteristics of deep convection over Darwin, Australia, *Mon. Weather Rev.*, *127*, 1056–1071, doi:10.1175/1520-0493(1999)127<1056:VVCODC>2.0.CO;2.
May, P. T., J. H. Mather, G. Vaughan, K. N. Bower, C. Jakob, G. M. McFarquhar, and G. G. Mace (2008), The tropical warm pool international cloud experiment, *Bull. Am. Meteorol. Soc.*, *89*(5), 629–645, doi:10.1175/BAMS-89-5-629.
McFarquhar, G. M., H. Zhang, G. Heymsfield, J. B. Halverson, R. Hood, J. Dudhia, and F. Marks (2006), Factors affecting the evolution of Hurricane Erin (2001) and the distributions of hydrometeors: Role of microphysical processes, *J. Atmos. Sci.*, *63*, 127–150, doi:10.1175/JAS3590.1.
Mlawer, E. J., S. J. Taubman, P. D. Brown, M. J. Iacono, and S. A. Clough (1997), Radiative transfer for inhomogeneous atmospheres: RRTM, a validated correlated-k model for the longwave, *J. Geophys. Res.*, *102*, 16,663–16,682, doi:10.1029/97JD00237.
Morrison, H., and J. Milbrandt (2011), Comparison of two-moment bulk microphysics schemes in idealized supercell thunderstorm simulations, *Mon. Weather Rev.*, *139*, 1103–1130.
Morrison, H., G. Thompson, and V. Tatarskii (2009), Impact of cloud microphysics on the development of trailing stratiform precipitation in a simulated squall line: Comparison of one- and two-moment schemes, *Mon. Weather Rev.*, *137*(3), 991–1007, doi:10.1175/2008MWR2556.1.
Petch, J. C., and M. E. B. Gray (2001), Sensitivity studies using a cloud-resolving model simulation of the tropical west Pacific, *Q. J. R. Meteorol. Soc.*, *127*(577), 2287–2306, doi:10.1002/qj.49712757705.
Petch, J. C., A. R. Brown, and M. E. B. Gray (2002), The impact of horizontal resolution on the simulations of convective development over land, *Q. J. R. Meteorol. Soc.*, *128*(584), 2031–2044.
Petersen, W. A., and S. A. Rutledge (2001), Regional variability in tropical convection: Observations from TRMM, *J. Clim.*, *14*, 3566–3586, doi:10.1175/1520-0442(2001)014<3566:RVITCO>2.0.CO;2.

Pinty, J.-P. (2002), A quasi 2-moment microphysical scheme for mixed-phase clouds at mesoscale with sensitivity to aerosols (CCN and IN), *11th Conference on Cloud Physics*, Am. Meteorol. Soc.

Pinty, J.-P., and P. Jabouille (1998), A mixed-phase cloud parameterization for use in a mesoscale non-hydrostatic model: Simulations of a squall line and of orographic precipitation, paper presented at Conference on Cloud Physics, Am. Meteorol. Soc., Everett, Wash.

Ramond, D. (1978), Pressure perturbations in deep convection: An experimental study, *J. Atmos. Sci.*, *35*, 1704–1711.

Randall, D. A., et al. (2003), Confronting models with data: The GEWEX cloud systems study, *Bull. Am. Meteorol. Soc.*, *84*(4), 455–469, doi:10.1175/BAMS-84-4-455.

Redelsperger, J.-L., et al. (2000), A GCSS model intercomparison for a tropical squall line observed during TOGA-COARE. Part I: CRM results, *Q. J. R. Meteorol. Soc.*, *126*(564), 823–863, doi:10.1002/qj.49712656404.

Rotstayn, L. D. (1997), A physically based scheme for the treatment of stratiform clouds and precipitation in large-scale models. I: Description and evaluation of the microphysical processes, *Q. J. R. Meteorol. Soc.*, *123*, 1227–1282.

Rotunno, R., and J. Klemp (1984), On the rotation and propagation of supercell thunderstorms, *J. Atmos. Sci.*, *42*(3), 271–292.

Schumacher, C., R. A. Houze Jr., and I. Kraucunas (2004), The tropical dynamical response to latent heating estimates derived from the TRMM precipitation radar, *J. Atmos. Sci.*, *61*, 1341–1358.

Shige, S., Y. N. Takayabu, S. Kida, W.-K. Tao, X. Zeng, C. Yokoyama, and T. L'Ecuyer (2009), Spectral retrieval of latent heating profiles from TRMM PR data. Part IV: Comparisons of lookup tables from two- and three-dimensional cloud-resolving model simulations, *J. Clim.*, *22*, 5577–5594.

Shutts, G. J., and M. E. B. Gray (1994), A numerical modeling study of the geostrophic adjustment process following deep convection, *Q. J. R. Meteorol. Soc.*, *120*(519), 1145–1178, doi:10.1002/qj.49712051903.

Simpson, J., T. D. Keenan, B. Ferrier, R. H. Simpson, and G. J. Holland (1993), Cumulus mergers in the maritime continent region, *Meteorol. Atmos. Phys.*, *51*, 73–99.

Skamarock, W. C., J. B. Klemp, J. Dudhia, D. O. Gill, D. M. Barker, M. G. Duda, X.-Y. Huang, W. Wang, and J. G. Powers (2008), A description of the advanced research WRF version 3, *NCAR Tech. Note*, *NCAR/TN-475+STR*.

Smith, P. L. (1984), Equivalent radar reflectivity factors for snow and ice particles, *J. Clim. Appl. Meteorol.*, *23*(8), 1258–1260, doi:10.1175/1520-0450(1984)023<1258:ERRFFS>2.0.CO;2.

Steiner, M., R. Houze, and S. E. Yuter (1995), Climatological characterization of three-dimensional storm structure from operational radar and rain gauge data, *J. Appl. Meteorol.*, *34*(9), 1978–2007.

Stephens, G. L. (2005), Cloud feedbacks in the climate system: A critical review, *J. Clim.*, *18*(2), 237–273, doi:10.1175/JCLI-3243.1.

Stevens, D. E., A. S. Ackerman, and C. S. Bretherton (2002), Effects of domain size and numerical resolution on the simulation of shallow cumulus convection, *J. Atmos. Sci.*, *59*(23), 3285–3301.

Stith, J. L., J. A. Haggerty, A. Heymsfield, and C. A. Grainger (2004), Microphysical characteristics of tropical updrafts in clean conditions, *J. Appl. Meteorol.*, *43*, 779–794, doi:10.1175/2104.1.

Stith, J. L., J. Haggarty, C. Grainger, and A. Detwiler (2006), A comparison of the microphysical and kinematic characteristics of mid-latitude and tropical convective updrafts and downdrafts, *Atmos. Res.*, *82*, 350–366.

Tao, W.-K., and M. W. Moncrieff (2009), Multiscale cloud system modeling, *Rev. Geophys.*, *47*, RG4002, doi:10.1029/2008RG000276.

Thompson, G., P. R. Field, R. M. Rasmussen, and W. D. Hall (2008), Explicit forecasts of winter precipitation using an improved bulk microphysics scheme. Part II: Implementation of a new snow parameterization, *Mon. Weather Rev.*, *136*, 5095–5115.

Thompson, R. L., R. Edwards, J. A. Hart, K. L. Elmore, and P. Markowski (2003), Close proximity soundings within supercell environments obtained from the Rapid Update Cycle, *Weather Forecasting*, *18*, 1243–1261, doi:10.1175/1520-0434(2003)018<1243:CPSWSE>2.0.CO;2.

Tiedtke, M. (1993), Representation of clouds in large-scale models, *Mon. Weather Rev.*, *121*, 3040–3061.

Uma, K. N., and T. Narayana Rao (2008), Characteristics of vertical velocity cores in different convective systems observed over Gadanki, India, *Mon. Weather Rev.*, *137*, 954–975, doi:10.1175/2008MWR2677.1.

Van den Heever, S. C., and W. R. Cotton (2004), The impact of hail size on simulated supercell storms, *J. Atmos. Sci.*, *61*, 1596–1609.

Van Weverberg, K., A. M. Vogelmann, H. Morrison, and J. Milbrandt (2012), Sensitivity of idealized squall-line simulations to the level of complexity used in two-moment bulk microphysics schemes, *Mon. Weather Rev.*, *140*, 1883–1907.

Van Weverberg, K., A. M. Vogelmann, W. Lin, E. P. Luke, A. Cialella, P. Minnis, M. Khaiyer, E. R. Boer, and M. P. Jensen (2013), The role of cloud microphysics parameterization in the simulation of mesoscale convective system clouds and precipitation in the Tropical Western Pacific, *J. Atmos. Sci.*, *70*, 1104–1128.

Varble, A., A. M. Fridlind, E. J. Zipser, A. S. Ackerman, J.-P. Chaboureau, J. Fan, A. Hill, S. A. McFarlane, J.-P. Pinty, and B. Shipway (2011), Evaluation of cloud-resolving model intercomparison simulations using TWP-ICE observations: Precipitation and cloud structure, *J. Geophys. Res.*, *116*, D12206, doi:10.1029/2010JD015180.

Vaughan, G., K. Bower, C. Schiller, A. R. MacKenzie, T. Peter, H. Schlager, N. R. P. Harris, and P. T. May (2008), SCOUT-O3/ACTIVE: High-altitude aircraft measurements around deep tropical convection, *Bull. Am. Meteorol. Soc.*, *89*, 647–662, doi:10.1175/BAMS-89-5-647.

Wang, Y., C. N. Long, L. R. Leung, J. Dudhia, S. A. McFarlane, J. H. Mather, S. J. Ghan, and X. Liu (2009), Evaluating regional cloud-permitting simulations of the WRF model for the Tropical Warm Pool International Cloud Experiment (TWP-ICE), Darwin, 2006, *J. Geophys. Res.*, *114*, D21203, doi:10.1029/2009JD012729.

Wei, D., A. M. Blyth, and D. J. Raymond (1998), Buoyancy of convective clouds in TOGA COARE, *J. Atmos. Sci.*, *49*, 1386–1395.

Wilhelmson, R. (1974), The life cycle of a thunderstorm in three dimensions, *J. Atmos. Sci.*, *31*, 1629–1651.

Wilson, D. R., and S. P. Ballard (1999), A microphysically based precipitation scheme for the UK Meteorological Office Unified Model, *Q. J. R. Meteorol. Soc.*, *125*, 1607–1636.

Wu, J., A. D. DelGenio, M.-S. Yao, and A. B. Wolf (2009), WRF and GISS SCM simulations of convective updraft properties during TWP-ICE, *J. Geophys. Res.*, *114*, D04206, doi:10.1029/2008JD010851.

Wu, X., and M. W. Moncrieff (2001), Sensitivity of single-column model solutions to convective parameterizations and initial conditions, *J. Clim.*, *14*(12), 2563–2582, doi:10.1175/1520-0442(2001)014<2563:SOSCMS>2.0.CO;2.

Wu, X., W. Grabowski, and M. Moncrieff (1998), Long-term behavior of cloud systems in TOGA COARE and their interactions with radiative and surface processes. Part I: Two-dimensional modeling study, *J. Atmos. Sci.*, *55*(17), 2693–2714.

Xie, S., et al. (2002), Intercomparison and evaluation of cumulus parameterizations under summertime midlatitude continental conditions, *Q. J. R. Meteorol. Soc.*, *128*(582), 1095–1135, doi:10.1256/003590002320373229.

Xie, S., T. Hume, C. Jakob, S. Klein, R. McCoy, and M. Zhang (2010), Observed large-scale structures and diabatic heating and drying profiles during TWP-ICE, *J. Clim.*, *23*(1), 57–79, doi:10.1175/2009JCLI3071.1.

Xu, K.-M., et al. (2002), An intercomparison of cloud-resolving models with the Atmospheric Radiation Measurement summer 1997 Intensive Observation Period data, *Q. J. R. Meteorol. Soc.*, *128*(580), 593–624, doi:10.1256/003590002321042117.

Xu, W. and E. J. Zipser (2012), Properties of deep convection in tropical continental, monsoon, and oceanic rainfall regimes, *Geophys. Res. Lett.*, *39*, L07802, doi:10.1029/2012GL051242.

Zeng, X., W.-K. Tao, S. Lang, A. Y. Hou, M. Zhang, and J. Simpson (2008), On the sensitivity of atmospheric ensembles to cloud microphysics in long-term cloud-resolving model simulations, *J. Meteorol. Soc. Jpn.*, *86A*, 45–65.

Zhou, Y. P., W.-K. Tao, A. Y. Hou, W. S. Olson, C.-L. Shie, K.-M. Lau, M.-D. Chou, X. Lin, and M. Grecu (2007), Use of high-resolution satellite observations to evaluate cloud and precipitation statistics from cloud-resolving model simulations. Part I: South China Sea Monsoon Experiment, *J. Atmos. Sci.*, *64*, 4309–4329, doi:10.1175/2007JAS2281.1.

Zhu, P., J. Dudhia, P. R. Field, A. Fridlind, A. Varble, E. Zipser, J. Petch, M. Chen, and Z. Zhu (2012), A limited area model (LAM) intercomparison study of a TWP-ICE active monsoon mesoscale convective event, *J. Geophys. Res.*, *117*, D11208, doi:10.1029/2011JD016447.

Zipser, E. J. (2003), Some views on "hot towers" after 50 years of tropical field programs and two years of TRMM data, *Meteorol. Monogr.*, *29*(51), 49–58.

Zipser, E. J., and C. Gautier (1978), Mesoscale events within a GATE tropical depression, *Mon. Weather Rev.*, *106*, 789–805.

Zipser, E. J., and K. R. Lutz (1994), The vertical profile of radar reflectivity of convective cells: A strong indicator of storm intensity and lightning probability?, *Mon. Weather Rev.*, *122*, 1751–1759, doi:10.1175/1520-0493(1994)122<1751:TVPORR>2.0.CO;2.